

BRILLOUIN SCATTERING FROM A GAS SUBJECT
TO A TEMPERATURE GRADIENT: OPTICAL
CONSIDERATIONS

CENTRE FOR NEWFOUNDLAND STUDIES

**TOTAL OF 10 PAGES ONLY
MAY BE XEROXED**

(Without Author's Permission)

CHIN HENG CHOO



**BRILLOUIN SCATTERING FROM A GAS SUBJECT
TO A TEMPERATURE GRADIENT: OPTICAL
CONSIDERATIONS**

By

ChinHeng Choo
B.Sc. (Hons.) Memorial University of Newfoundland

A THESIS SUBMITTED IN PARTIAL FULFILLMENT OF THE
REQUIREMENTS FOR THE DEGREE OF MASTER OF SCIENCE

DEPARTMENT OF PHYSICS AND PHYSICAL OCEANOGRAPHY
MEMORIAL UNIVERSITY OF NEWFOUNDLAND

AUGUST 1996

ST. JOHN'S

NEWFOUNDLAND



National Library
of Canada

Acquisitions and
Bibliographic Services Branch

395 Wellington Street
Ottawa, Ontario
K1A 0N4

Bibliothèque nationale
du Canada

Direction des acquisitions et
des services bibliographiques

395, rue Wellington
Ottawa (Ontario)
K1A 0N4

Your file Votre référence

Our file Notre référence

The author has granted an irrevocable non-exclusive licence allowing the National Library of Canada to reproduce, loan, distribute or sell copies of his/her thesis by any means and in any form or format, making this thesis available to interested persons.

The author retains ownership of the copyright in his/her thesis. Neither the thesis nor substantial extracts from it may be printed or otherwise reproduced without his/her permission.

L'auteur a accordé une licence irrévocable et non exclusive permettant à la Bibliothèque nationale du Canada de reproduire, prêter, distribuer ou vendre des copies de sa thèse de quelque manière et sous quelque forme que ce soit pour mettre des exemplaires de cette thèse à la disposition des personnes intéressées.

L'auteur conserve la propriété du droit d'auteur qui protège sa thèse. Ni la thèse ni des extraits substantiels de celle-ci ne doivent être imprimés ou autrement reproduits sans son autorisation.

ISBN 0-612-17579-0

Canada

Abstract

This thesis describes an attempt to use the Brillouin light scattering technique to observe nonequilibrium effects in gaseous sulphur hexafluoride subject to a temperature gradient. Due to the inherent geometry of the experimental setup, an imaging fibre optic probe was investigated as a means of scattered light collection. The SF₆ gas was housed in a moderate pressure gas cell. The scattered light collected was analyzed with a Fabry-Perot interferometer. A computer simulation of the behaviour of temperature, density and refractive index for gaseous SF₆ subject to a temperature gradient was performed using a 2 dimensional nonconvective heat flow model. A computer simulation of the scattered ray paths from the gas cell to the optical fibre in the imaging fibre optic probe was also performed. The sound speed in SF₆ at a pressure of 1.28 MPa and a temperature of 20°C was measured to be $133 \pm 6 \text{ m}\cdot\text{s}^{-1}$. Sound speeds in SF₆ for pressures from 0.44 MPa to 1.83 MPa were also measured. These sound speeds showed a larger nonlinearity in its changed with different pressures than that calculated from theory. Nonequilibrium Brillouin spectra for SF₆ were observed at pressures of 0.891 MPa and 1.35 MPa with temperature gradients of about 15.3 K cm^{-1} and 18.9 K cm^{-1} , respectively. The Brillouin components at nonequilibrium showed an intensity increase of about 16% when compared to their counterparts at equilibrium.

Acknowledgements

I wish to thank my supervisors, Dr. M.J. Clouter and Dr. H. Kiefte for sharing with me their expertise in the field of light scattering and for their guidance throughout the course of this research and the preparation of this thesis. I would also wish to thank Dr. J.C. Lewis for suggesting the method used in the computer simulation of the temperature and density gradients in this thesis.

I would wish to thank Mr. Todd Andrew for sharing with me his knowledge on light scattering and all others who have assisted me in the completion of this project.

While engaged in this work I was supported by a Memorial University Graduate Fellowship which I gratefully acknowledge.

Table of Contents

Abstract	i
Acknowledgements	ii
Table of Contents	iii
List of Figures	vi
1. Introduction	1
1.1 Nonequilibrium Fluid	1
1.2 Brillouin Scattering in a Gas	1
1.3 Theory of Light Scattering in a Nonequilibrium Fluid	5
1.3.1 Sound Bending	6
1.4 Scattering Geometry	10
2. Experimental Method	14
2.1 Introduction	14
2.2 Input Optics	14
2.3 Reference Optics	16
2.4 Collection Optics	18
2.5 Input End	19
2.5.1 Imaging Fibre Optic Probe	19
2.5.2 Output End	27
2.6 The Gas Scattering Cell	31

3. Simulation of Scattered Ray Paths in a SF₆ Gas	
with a Density Gradient	34
3.1 Introduction	34
3.2 The Sulphur Hexafluoride Gas	35
3.3 Computer Simulation of the Density Distribution in a Temperature Gradient	38
3.4 Raytracing Through the Density Gradient and the Imaging Fibre Optic Probe	44
3.4.1 Raytracing Through the Density Gradient	44
3.4.2 Raytracing Through the Imaging Fibre Optic Probe	47
4. Experimental Results	53
4.1 Introduction	53
4.2 Results	53
5. Discussion	65
5.1 Discussion	65
5.2 Conclusion	68
Bibliography	71
Appendix A	74
Physical Properties of Sulphur Hexafluoride	
Appendix B	76
Propagative Modes in an Optical Fibre	

Appendix C	79
Inelastic Light Scattering	
Appendix D	83
Program Flowcharts and Source Codes	

List of Figures

1. Brillouin intensity effects for fluid in different nonequilibrium conditions	4
2. Simple sound bending	7
3. Total sound bending	8
4. Computer simulation of sound speed	11
5. Cavity modes in a lasing medium linewidth	14
6. Horizontal and vertical amplitude profile of laser beam	15
7. Argon ion laser light properties	16
8. Input, Reference and Input End of Collection Optics	17
9. Guiding light through the optical fibre	19
10. The Imaging Fibre Optic Probe	20
11. Transmittance curve for a fused silica single fibre	22
12. Modes seen from optical fibre	23
13. Image distances at various object distances	24
14. Magnification factor for various object distances	24
15. Coupling light rays at maximum efficiency	25
16. Output section of Collection Optics	26
17. Gas Scattering Cell	32
18. Vapour pressure curve of SF ₆	35
19. 2-D nonconvective heat flow model	38
20. Density distribution as a function of height	42

21. Density distribution as a function of temperature	42
22. Temperature distribution as a function of height	43
23. Refractive index distribution as a function of height	43
24. Axial cross sectional geometry of gas scattering cell and aperture	44
25. Computer simulation output: scattered ray paths through a density gradient	45
26. Computer simulation output: scattered ray paths through the aperture	46
27. Transfer function coordinates	47
28. Vector diagram for light refraction	49
29. Computer simulation output: scattered ray paths through imaging fibre optic probe	51
30. Simulated frequency distribution of collected scattered light	52
31. A Brillouin spectrum collected for SF ₆ gas in an equilibrium state	54
32. The Brillouin spectrum for one order of interference	54
33. Linewidth of a Brillouin component	55
34. Changes in X-peaks position as FSR changes	56
35. Frequency shift (channels) versus plates separation plot	57
36. Changes in the characteristics of X-peaks as pressure is changed	59
37. 158° backscatter Brillouin shifts for different pressures	60
38. Frequency shifts of X-peaks and backscatter peaks for different pressures	61
39. Sound speeds in gaseous SF ₆ for different pressures	61

40. Brillouin spectrum of both equilibrium and nonequilibrium states: Pressures from 0.919 MPa to 0.891 MPa	62
41. Brillouin spectrum of both equilibrium and nonequilibrium states: Pressures from 1.38 MPa to 1.35 MPa	63
42. Equilibrium and nonequilibrium conditions with respect to the vapour pressure curve	64
A.1 Different propagative modes	77
A.2 The first ten LP_{0j} modes	77
A.3 Effect of fibre diameter on wave speed for the HE_{11} , TE_{10} and TM_{10} modes	78
A.4 Inelastic light scattering	80
A.5 Vector addition of wavevectors in inelastic light scattering	81
A.6 Rotation of aperture's coordinate	107

To the memory of my father,

Mr. Choo PengYoong

Chapter 1

Introduction

1.1 Nonequilibrium fluid

Although systems in equilibrium in general are well studied, progress in the analysis of systems in nonequilibrium states is often slow either because of the lack of a theory to properly explain existing experimental data or the lack of experimental evidence to support and verify results from theories that attempt to explain these behaviours. In this thesis, I will discuss an attempt to observe nonequilibrium effects in a gas subject to a temperature gradient by investigating changes in the interactions between light and sound waves (phonons) as the gas goes from an equilibrium to a nonequilibrium state. Brillouin (light) scattering techniques will be used in this experiment to probe for these effects in a scattering geometry that is different from previous experiments of this nature.

1.2 Brillouin Scattering in a gas

Spontaneous microscopic fluctuations always exist in any system whose temperature is above absolute zero. These microscopic fluctuations dissipate in the same way as external perturbations do. Local fluctuations interact with each other to produce collective fluctuations with a distribution of wavelengths and frequencies. By studying these collective thermal fluctuations, we can extract important thermodynamic properties and transport coefficients like the ratio of specific heats γ , the adiabatic sound velocity, isothermal compressibility χ , thermal diffusivity, thermal conductivity and coefficients of viscosity. These thermal fluctuations are also called thermal sound waves.

Since these thermal fluctuations present themselves in a distribution of wavelengths, different techniques may be required to study fluctuations at regions with different wavelengths and frequencies. At low frequencies and long wavelengths, these thermal fluctuations behave like a continuum and can be modeled by hydrodynamic theory. But at wavelengths that are comparable to the molecular mean free path, local molecular structure

of the fluid becomes important, and the fluctuations no longer behave like a continuum. This is the molecular dynamic regime. The hydrodynamic regime is characterized by low wavenumber k and frequency ω , and also by a parameter $y \gg 1$ [45]. $y = \lambda/l$ where λ is the wavelength of fluctuations and l is the mean free path. The molecular dynamic regime is characterized by higher k and ω and $y \ll 1$. For $y \ll 1$, we have free particle motions.

To study the behaviour of thermal fluctuations in the hydrodynamic regime, we can use either the Brillouin (light) scattering or ultrasonic techniques. Ultrasonic techniques can only study fluctuations confined to a regime of very low k and ω whereas light scattering techniques allow us to study fluctuations over a much wider range of k and ω . In Brillouin scattering, the interaction between an incident photon and the fluctuations (phonons) gives rise to a momentum transfer and a photon of a different wavelength is scattered (see Appendix C for more detail). The wavelength of the momentum transfer is $\lambda = \lambda_0 / (2n \sin(\theta/2))$, where λ , λ_0 and θ specify the wavelength of the fluctuations, wavelength of incident light and scattering angle respectively. The angular frequency shift of the scattered light would be $\pm\omega$,

$$\omega = ck = \frac{4\pi n}{\lambda_0} \sin \frac{\theta}{2}, \quad (1)$$

where c is the speed of the sound waves and n is the refractive index. If ω_0 corresponds to the angular frequency of the incident light or the Rayleigh line, then $\omega_0 + \omega$ and $\omega_0 - \omega$ would correspond to the upshifted and downshifted Brillouin lines. The Brillouin lines would appear as satellites on either side of the Rayleigh line in the spectrum. Since it is common practice to specify the Brillouin shifts in term of frequency, $f = \frac{\omega}{2\pi}$ rather than its angular frequency, we shall use f for our frequency shifts unless stated otherwise. In the experiments reported herein, we will be using Brillouin scattering techniques to probe for nonequilibrium effects in a dense gas with a forward scattering geometry, thus probing for sound waves in the hydrodynamic regime.

The above mentioned concept of elastic (or sound) waves in a continuous medium was introduced by Debye in his theory of solid state thermal capacity. These elastic waves

are essentially normal modes arising from the interaction of vibrating particles in a solid crystal lattice. The interactions between light and sound waves to produce scattered light that possesses two frequency shifted components were independently predicted by Brillouin[1] in 1922 and Mandelstam[2] in 1926. They were subsequently observed by Gross[3] in 1930 in a monocrystal of quartz. He later also observed the frequency shifted Brillouin component in a liquid. Even though there were attempts to observe Brillouin scattering in gaseous H₂, N₂ and O₂ as early as 1942[4], the first successful observation of the Brillouin components in a gas did not come till 1965 in a stimulated Brillouin scattering experiment [5]. In the following year, spontaneous Brillouin scattering was observed in Ar, Xe, N₂, CO₂ and CH₄ [6]. Even though particles in a gas do not vibrate about a well define location like in a crystal lattice, sound waves can still exist in a gas as long as the gas to be considered can be treated as a continuous medium. In this case, the wavelength of the sound waves probed have to be much longer than the mean free path of the particles in the gas [7]. We have

$$\lambda \gg l ,$$

$$\lambda \gg \frac{1}{\sqrt{2}\pi d^2 \rho} , \quad (2)$$

where d is the molecular diameter and ρ is the number of molecules per unit volume. Since pressure is directly related to density, observation of a Brillouin spectra will get progressively more difficult as the pressure of the gas gets lower until we reach a stage where $\lambda \sim l$, when the Brillouin lines would not longer exist.

Not only can Brillouin scattering techniques be used to determine behaviours of various thermodynamic properties in a system in equilibrium, given the right conditions these scattering techniques can also be used to observe the behaviour of a system not in equilibrium. Although nonequilibrium effects have been observed in both solid and liquid [8], I will confine my discussion to just the effects in a nonequilibrium fluid; as most of the theories put forward so far on light scattering in a nonequilibrium system are for a

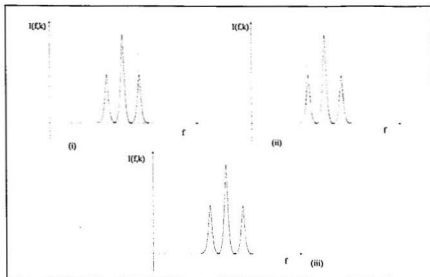


Figure 1 Brillouin intensity effects for fluid in different non-equilibrium conditions

non-equilibrium fluid. A non-equilibrium state in a fluid may be achieved by several means, as follows,

- i) Subjecting a fluid to a temperature gradient.
- ii) Inducing a macroscopic velocity gradient in the fluid.
- iii) Inducing a difference between the rotational and translational gas temperatures in the fluid.

The non-equilibrium effects for these different conditions are shown in Figure 1. For a fluid in a non-equilibrium state created through conditions ii) and iii), an equal change in both the upshifted and downshifted Brillouin lines will be observed [9]. For a fluid subjected to a temperature gradient, the effect on the Brillouin lines will be an equal but opposite change in the intensity of Brillouin lines, i.e. there will be an asymmetry about the Rayleigh line, in the intensity between the upshifted and downshifted Brillouin lines. In this case, the sound waves propagate along the direction of the temperature gradient. A non-equilibrium effect that is similar to that of a fluid existing in condition ii) can also be seen in a fluid with a temperature gradient if the sound waves that are probed are propagating in a direction

perpendicular to that probed in the previous scattering geometry [10].

1.3 Theory of light scattering in a nonequilibrium fluid

There have been several theories, prior to [10], proposing to explain the asymmetric Brillouin spectrum in a nonequilibrium fluid [11 - 15]. These theories attempt to calculate the dynamic structural factor (which is related to the intensity of the Brillouin lines) in a nonequilibrium fluid in stationary state subjected to a small steady heat flux. By looking at this system for a state slightly perturbed from equilibrium, they were able to deduce an intensity difference between the upshifted and downshifted Brillouin lines, corrected to the linear order in the temperature gradient. These are due to the so-called mode-coupling effects. The Brillouin intensity can be separated into two parts, a local equilibrium part and a mode-coupling part:

$$J_{Bs} = J_{Bs}^{LE} + J_{Bs}^{MC}. \quad (3)$$

J_{Bs} and J_{Bs} are the upshifted and downshifted Brillouin component, respectively. Any effects from the nonequilibrium fluid would come from the mode coupling part J_{Bs}^{MC} , which may cause the total integrated intensity of the upshifted or downshifted line to be higher or lower than the total integrated intensity at local equilibrium.

The results from the linear theory were verified by experiments done on water by H. Kiefte, M.J. Clouter and R. Penny [8]. These experiments were carried out in conditions where spatial inhomogeneities over the sound attenuation length and boundary effects can be neglected. A similar older experiment performed by Beysens, Garrbos and Zalczer [16] where conditions were not as "ideal" yield data that cannot be accounted for by the linear theory. Newer theories were later proposed to account for the results from both these experiments. A theory from Satten and Ronis [17] incorporated boundary conditions into the linear theory while another from Kirkpatrick et al [18] uses a nonlinear theory that takes into consideration the spatial inhomogeneities in the nonequilibrium fluid but neglects boundary effects. The results from both the experiments were consistent with these two theories, to within a large uncertainty in the data. Thus, even though the theories were able to account for the results, they were not able to point to the actual effect that explains the results of the

experiments. The underlying mechanism that causes the deviation of results from the earlier linear theory may be nonlinear or boundary by nature, or it may be a combination of both of these effects.

A general theory proposed by Schmitz and Cohen [10], intends to resolve this ambiguity by incorporating both the boundary and nonlinear effects into their theory for nonequilibrium fluid. It was hoped that through this theory, different degrees of boundary and nonlinear effects can be adjusted to explain the experimental results. The nonlinearity of this theory requires that thermal sound waves produced from spontaneous fluctuations do not propagate in a straight line path as was in the linear theory, but rather because of spatial inhomogeneity, the sound waves now propagate along curve paths, i.e the sound rays are now bent. Since the linear theory and the nonlinear theory are just limiting cases of this general theory, probing the sound waves from different scattering geometry in the nonequilibrium fluid, as predicted from this theory, would allow us to probe for nonequilibrium effects from one regime to another. By probing sound waves with vectors in the vertical direction (along the direction of ∇T), we can look for nonequilibrium effects in the linear regime without boundary effects whereas probing sound waves with vectors in the horizontal direction (perpendicular to the direction of ∇T) would allow us to investigate nonlinear effects, like sound bending, in the nonequilibrium fluid.

These nonlinear effects on the Brillouin lines intensity are investigated in this experiment in the hope to validate this general theory for nonequilibrium fluid. Briefly, the theory of sound bending and the results for Brillouin line intensity as calculated for the horizontal scattering geometry will be discussed in the following section.

1.3.1 Sound bending

When the nonlinear effects are considered in the general theory of nonequilibrium fluid proposed by Schmitz and Cohen, spatial inhomogeneities are not ignored, thus affecting the sound speed as it propagates through the nonequilibrium fluid. The author have through the application of WKB techniques to the equations of fluctuating hydrodynamics, found that thermal sound waves produced from spontaneous fluctuations no longer propagate along straight ray paths, the ray paths are now bent to curves, as shown in Figure 2. This is similar to sound propagation in a stratified medium. A ray can be uniquely characterize if

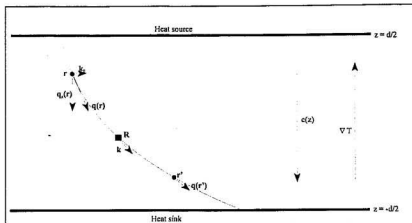


Figure 2 Simple sound bending

its wavevector k and its scattering position R are known. Any position along the ray path is characterized by its tangential vector $\vec{q}(\vec{r})$ as follows,

$$\vec{q}(\vec{r}) = \vec{q}(\vec{r}, \vec{R}, \vec{k}) = (k_y, q_z(\vec{r}, \vec{R}, \vec{k})) \quad (4)$$

Since, the horizontal component of \vec{k} , k_x is conserved along the ray path, we can write Snell's law in terms of the magnitude of the vectors,

$$c(z)q(\vec{r}, \vec{R}, \vec{k}) = c(R_2)k, \quad (5)$$

where $c(z)$ is the speed of the sound wave along the ray path at position z and $c(R_2)$ is the speed of the sound wave at z position of vector \vec{R} . The sound waves would also experience the total internal reflection effect if the following criterion is met:

$$c(z) \frac{k_x}{k} > c(R_2) \quad (6)$$

The authors refer to z values characterized by (6) as a "forbidden region". If the forbidden

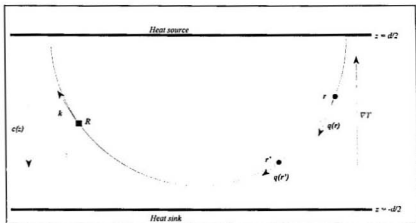


Figure 3 Total bending, sound waves originating from heat source return to the heat source.

region is empty, then rays are monotonically bent as shown in Figure 2. But if it is not empty, then rays are deviated to the opposite z direction at the point where they touch the forbidden region in the fluid, and propagate back to the plate¹ where they originated, as shown in Figure 3. The authors refer to this phenomenon as “total sound bending”.

Other than the need for the sound bending effect, the general theory also requires the modification of the concept of constant sound attenuation length. Since the speed is not constant, the sound damping coefficient $\Gamma_s(z)$ would no longer be constant too, thus the attenuation length l , which is

$$l(R_s, k) = \frac{2c(R_s)}{\Gamma_s(R_s)k^2}, \quad (7)$$

needs to be subsequently modified too. For $l \ll L_p$, where L_p is the length over which the macroscopic properties of the fluid change, nonlinear effects may be ignored.

¹From Figure 2, “plate” here refers to either the heat source or heat sink.

$$L_T^{-1} = \left(\frac{\partial \ln a}{\partial T} \right) \frac{dT}{dz}, \quad (8)$$

where $a(T)$ stands for the thermodynamic or transport coefficient that depends most sensitively on temperature. In our case, a can be the speed of sound $c(z(T))$. Since the temperature gradient and the magnitude of the sound speed gradient increase rapidly as z gets close to the bottom of the cell, we can expect L_T to decrease rapidly at that point too.

In a vertical scattering geometry, the sound waves probed have vectors with $|k_z| = 1$, they propagate in a straight line along the vertical direction. In vertical scattering, one can probe for nonequilibrium effects in the linear regime, as was done in the previous experiments [8]. For a horizontal scattering geometry, we have $|k_z| = 0$, and one can probe for nonlinear effects like total sound bending at the position where the ray just touches the forbidden region. The authors have found the mode-coupling contributions to the Brillouin line intensity as follows,

$$I_{B\pm}^{MC}(k; R_z) = I_B(R_z) \frac{1}{T(R_z)} \int_{R_z}^{-\left(\frac{d}{2}\right) \text{sgn} \frac{dc}{dz}} \frac{dc}{dz} \frac{dT}{dz} \exp \left[-2 \int_z^{R_z} dz' \frac{1}{l(z', k)} \frac{1}{[1 - c^2(z')/c^2(R_z)]^{\frac{1}{2}}} \text{sgn} \frac{dc}{dz} \right], \quad (9)$$

where $\text{sgn} \frac{dc}{dz}$ is the sign of $\frac{dc}{dz}$. Equation (9) may be evaluated explicitly to the lowest order in the temperature gradient to give the following result,

$$I_{B\pm}^{MC} = -I_B(R_z) \frac{1}{T^2(R_z)} \left(\frac{dT}{dR_z} \right)^2 \frac{d \ln c}{d \ln T}(R_z) \frac{I^2}{4}(R_z, k) [1 - C(k)], \quad (10)$$

where $I_B(R_z)$ is the local equilibrium Brillouin line intensity, and $C(k)$ is the finite size correction given in [10]. The mode-coupling contribution in this case is the same for both the upshifted and the downshifted line. The nonequilibrium effect in this case would be a

change in the total intensity of both the Brillouin lines when the fluid is moved from an equilibrium state to a nonequilibrium one. From the results in Equations (9) and (10), a large temperature gradient $\frac{dT}{dz}$ or a large change in sound speed along z , $\frac{dc}{dz}$, together with sound waves with small k would produce a large nonlinear effect in the Brillouin line intensities. In this experiment, we would attempt to create a large nonlinear effect in the nonequilibrium fluid by inducing a large $\frac{dc}{dz}$. For sound propagation in sulphur hexafluoride gas, the speed of sound waves is related to the density as follows [19].

$$c^2 = \Upsilon \frac{RT}{M} \left[1 + 2\rho \frac{B(T)}{0.146} \right], \quad (11)$$

where R is the gas constant, M is the molecular weight, ρ is the density, Υ is the ratio of the specific heats c_p and c_v , and $B(T)$ is the second virial coefficient of the virial expansion of the equation of state. Equation (11) is valid for densities up to 100 kg m^{-3} and temperatures from 230 K to 1200 K. From Equation (11), we can see that a large density gradient along z would induce a large change in the sound speed along z . The large density gradient can be created by working with temperatures that are close to the vapour pressure curve of the gas. This is done in our experiment by creating a temperature gradient such that the lowest temperature in the gradient is very close to the vapour pressure point of the gas held at a particular pressure. A computer simulation of the sound speed for different z along the height of the cell is shown in Figure 4. In this simulation Equation (11) uses data from the temperature and density gradient simulation from Chapter 3. Because of the approximations employed, the behaviour of $c(z)$ near the origin in Figure 4 is not expected to be accurate.

We hope that by coupling a moderate temperature gradient with a large sound speed gradient in addition to looking at scattering at small angles, we would be able to observe the nonlinear effects as required by the general theory for a nonequilibrium fluid.

1.4 Scattering geometry

Due to the inherent geometry of this experimental setup, the use of conventional optical techniques (i.e. apertures, lenses and mirrors mounted on optical tracks) to collect scattered light would be difficult. One of these difficulties stems from the space restrictions arising from the need to look at forward scattering along the direction of the density gradient.

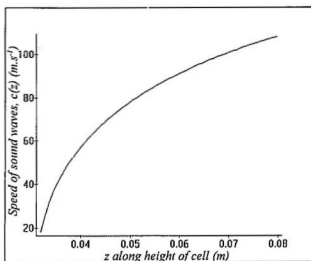


Figure 4 Computer simulation of sound speed along height of cell according to the approximations of Chapter 3.

The density gradient is created in a gas scattering cell, so in order to look at forward scattering along the gradient, we would need to position the collection optics beneath the gas cell. Another difficulty relates to the need to look at scattering from various scattering angles. Because of this, we would need an optical setup that would allow us to easily realign the optic axis of the collection optics along the different scattering angles. To use conventional optical techniques under these circumstances would be difficult. Therefore the use of an imaging fibre optic probe was investigated as a means of collecting scattered light from our experimental setup. The imaging fibre optic probe is made up of an aperture, an optical fibre and a set of imaging optics that focusses the scattered light from the cell into the optical fibre.

The use of optical fibres for scattered light collection has its roots in Dynamic Light Scattering (DLS). DLS is the scattering of light from an ensemble of macromolecules or particles that move under Brownian motion. Under this random motion, the intensity of scattered light from these particles fluctuates with time. Information about the particles' size and size distribution can be obtained from the time scale of the intensity fluctuations. The

use of optical fibre techniques in DLS was first demonstrated by Tanaka and Benedek in 1975 [20] and later developed further by Dyott in 1978 [21]. There are various designs for the fibre optic probe used in fibre optic based DLS experiments, they range from simple lens/fibre bundle to graded index (GRIN) lens/single mode fibre [22] combinations. The design of a fibre optic probe essentially consists of an imaging lens system that focusses scattered light into the optical fibre to within the solid angle specified by its acceptance cone. Apertures and spatial filters may be incorporated into the design to reduce noise and angular uncertainty in the scattered light collected.

The use of optical fibre techniques as a means of scattered light collection and delivery for Raman and Brillouin scattering was discussed by Brown in 1987 [23]. The use of optical fibre in Raman spectroscopy was initiated by Eckbreth in 1979[24]. Since there are no angular dependence of the frequency shifts in Raman spectroscopy, the range of scattering angles collected by optical fibre techniques may be as large as that defined by the acceptance cone of the fibre. For this reason, apertures and lenses may not be required for some Raman scattering experiments [25] whereas Brillouin scattering experiments would most definitely require the use of these components. This is because of the dependence of its frequency shifts on the scattering angles, a wide range of scattering angles would mean a large linewidth in the Brillouin spectrum.

Although optical fibre techniques similar to those in DLS experiments, to my knowledge, have not been applied in Brillouin spectroscopy before, there are many Brillouin scattering experiments that have been performed on the optical fibre itself. In this case the optical fibre is used both as the sample to be studied (for 90° and 180° scattering) and as a means of channeling scattered light from inside the fibre to the detection optics (180° scattering), and no fibre optic probe is used for scattered light collection. One of these experiments was done in 1972 with simulated Brillouin scattering in a single mode glass fiber by Ippen and Stolen [26]. They were able to measure a backscatter frequency shift of 32.2 GHz with a Fabry-Perot interferometer. Another similar experiment, that uses the Brillouin gain method of measuring the frequency shift, was done by Azuma et al [27] in 1988. They were able to measure the backscatter Brillouin shifts of the fibres down to 10.4 GHz and Brillouin linewidths down to 101 MHz. A Spontaneous Brillouin scattering

experiment with single mode fibre was done in 1983 by Stone and Chraplyvy [28]. They measured the backscatter Brillouin shift to be 12.7 GHz using a Fabry-Perot interferometer. Other experiments were done to measure the shifts at 90° scattering angle, but as mentioned before, the fibre is used only as a sample [29]. Heterodyne detection technique has also been used to observed spontaneous backward Brillouin scattering in an optical fibre [30].

In this thesis, I would present a method of scattered light collection and delivery that is applicable to both forward and backward Brillouin scattering. Scattered light is collected by the imaging fibre optic probe² and delivered to a single pass Fabry-Perot interferometer for spectral analysis, using a multimode optical fibre. The compactness of the imaging fibre optic probe and the flexibility of the optical fibre would allow us to easily align the optic axis of the probe to different positions and scattering angles. We were able to measure the spontaneous Brillouin shifts of gaseous sulphur hexafluoride down to about 98.5 MHz and the width of the Rayleigh line to about 50.5 MHz.

² Refers to the fibre optic probe used in our experimental setup.

Chapter 2

Experimental Method

2.1 Introduction

As in most light scattering experiments, our experimental setup consists essentially of optics to

- i) direct the laser light from a source to a sample and
- ii) collect scattered light from the sample for spectral analysis.

We have also added an extra set of optics for directing a reference beam through the sample and into the collection optics so as to actively optimize the Fabry-Perot interferometer for spectral analysis. Altogether, we have 3 sets of optics, one to direct the laser light to the sample, called the Input Optics, another to collect and analyze the scattered light, called the Collection Optics and finally one for directing and controlling the reference beam called the Reference Optics.

2.2 Input Optics

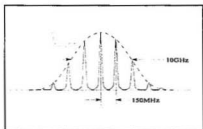


Figure 5 Cavity modes in a lasing medium line width.

The laser light used in our light scattering experiment is generated from a Coherent Innova 90 Argon ion laser. The laser is set up to operate at the green argon line of 514.5 nm using the model 934 Wavelength Selector. The lasing medium line width is about 10 GHz

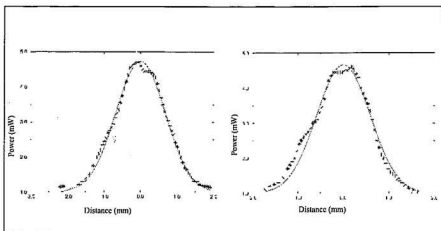


Figure 6 The horizontal (left) and vertical (right) amplitude profile of the laser beam at a distance of about 2 metres away from the output coupler. Both the profiles are fitted to gaussian functions.

(8.83×10^{-3} nm). This laser line is, however, modulated by the resonant cavity in such way that cavity modes of much smaller line widths are present. This is shown in the Figure 5. For a resonant cavity of refractive index 1 and a length of about 1 metre, we have cavity modes that are spaced about 150 MHz apart. To select only one of these modes for laser output, we use a solid fused quartz etalon placed in the laser (resonant) cavity. This etalon acts as a filter to select only one mode for single frequency (single longitudinal mode) operation in the laser. Since the etalon maximum transmission frequency is temperature dependent ($5.2\text{GHz}/^\circ\text{C}$), it is housed in a temperature controlled optic mount for minimum frequency drift. The transverse mode of our laser light is the TEM_{00} mode, an amplitude profile of this laser beam mode at a distance of about 2 metres away from the output coupler is shown in Figure 6. The power of the laser light used in our experiment ranges from about 140 mW to about 160 mW. Some of the other properties of the laser light are shown in Figure 7.

The optics used for directing the laser light from the laser to the gas scattering cell is shown in Figure 8. The half-wave plate that is positioned just after the laser is used to orientate the polarization of the laser beam in such a way that the polarization of the

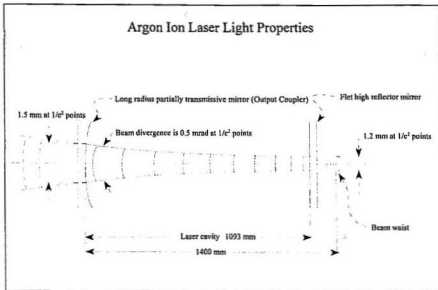


Figure 7 Argon ion laser light properties

scattered light emerging from the cell is perpendicular to the direction of the optic axis of the imaging fibre optic probe. After leaving the half-wave plate, the laser beam is subsequently directed into a biconvex lens that focuses the laser beam into a region at the lower part of the cell, in a location where we want the observed scattering to take place. After leaving the biconvex lens, the laser beam is directed into the cell through 2 adjustable mirrors, one to direct it along the y axis towards the gas cell and another to direct it down the gas cell. To align the laser beam to go through the gas cell in a direction that is perpendicular to both the top and bottom windows, we use a plane mirror. The beam is first aligned with the mirror placed on the top of the cell, then aligned again with the mirror placed below the gas cell. In both instances, the path of the reflected beam is adjusted to coincide with the path of the incident beam. The beam splitter that is positioned after the biconvex lens taps off a secondary (reference) beam of light and directs it into the Reference Optics, as shown in Figure 8.

2.3 Reference Optics

After the reference beam leaves the main laser beam, it is attenuated by an etalon

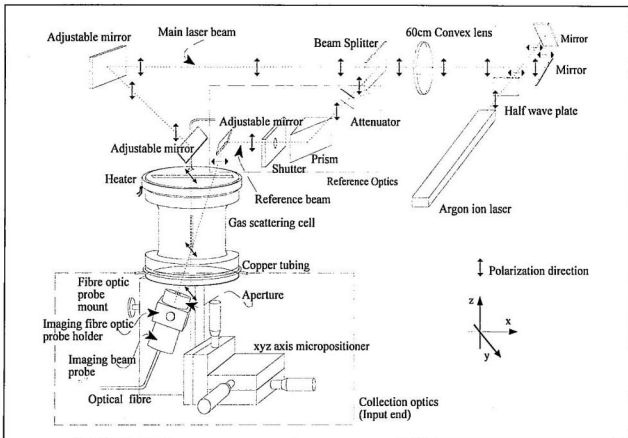


Figure 8 Input, Reference and Input End of Collection optics

filter (for 514.5 nm wavelength). By positioning the filter at different angles to the reference beam, the reference beam can be attenuated to different degrees. Least attenuation occurs when the filter is perpendicular to the reference beam, but attenuation increases as we tilt the filter position away from the perpendicular position. Attenuation is required for the reference beam because the intensity of an unattenuated beam would overwhelm the photomultiplier tube with photons, making it impossible to detect and optimize on the Rayleigh line.

A prism is used to direct the reference beam through a computer controlled shutter onto an adjustable mirror. The computer controlled shutter is opened for a period that is of order 1/16th the total time spent in one scan of the spectrum. The reference beam is shut off for the rest of the scan so that the reference beam would not overwhelm the Brillouin lines. The adjustable mirror after the shutter would then direct the reference beam through the gas cell and into the imaging fibre optic probe. Again, a plane mirror is used to align the reference beam into the gas cell. The reference beam is also used to fairly accurately determine the scattering angle for the collection optics. This is done by first removing the imaging beam probe from the imaging fibre optic probe, leaving behind only the aperture. In this case, an aperture 25.4 mm in length and 1.59 mm in diameter is used. The aperture position is then adjusted either by using the xyz axis micropositioner and/or rotating the aperture about its axis in the imaging fibre optic probe mount. The position is adjusted so that a maximum amount of light from the reference beam gets through. We record the x and z micrometer position in the micropositioner. Next, we move the aperture to another x and z position that would again allow the maximum amount of light through and record its position again. Since we are essentially moving along the reference beam path, knowing the coordinates of this path at two different position would allow us to easily calculate the angle between the reference and the main beam in the cell. This calculated angle also gives us the angle of the scattered light collected. The reference beam should also not be attenuated in this case, because we want the beam spot to be seen as clearly as possible after passing through the aperture.

2.4 Collection Optics

The collection optics is comprised of a set of input optics which collects scattered light into an optical fibre and a set of output optics which directs the scattered light through

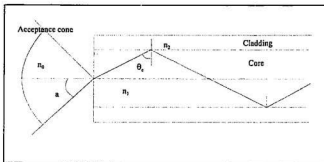


Figure 9 Guiding light through the optical fibre

the Fabry-Perot interferometer for spectra analysis. Theoretically, they can be as far away as needed, provided we have an optical fibre long enough to link them together.

2.5 Input End

The imaging fibre optic probe is the central component of the input end of the collection optics. It collects the scattered light from the cell and channels it to the output end for analysis. In the following section, I will discuss in detail, the design and workings of the imaging fibre optic probe.

2.5.1 Imaging Fibre Optic Probe

The imaging fibre optic probe is made up of an imaging beam probe from Oriel, a multimode single optical fibre and an aperture attachment, with or without the polarizer film. This is shown in Figure 10. Because the optical fibre serves as a conduit for scattered light from the imaging fibre optic probe to the Fabry-Perot interferometer, it is important for us to know how the optical fibre would modify the scattered light as it enters and propagates through the fibre. Therefore, I will start off this section with a short discussion of some of the basic principles of optical fibre operations.

Light is guided through an optical fibre by total internal reflection. The optical fibre is made up of a core that is surrounded by a cladding, as shown in Figure 9. In order for total internal reflection to take place, the refractive index of the core must be greater than that of the cladding. Angle α is the incident angle at which a light ray entering the fibre would produce a refracted ray that would be incident on the cladding and core interface at critical angle. Any incident angle that is larger than α would produce a refracted ray that is

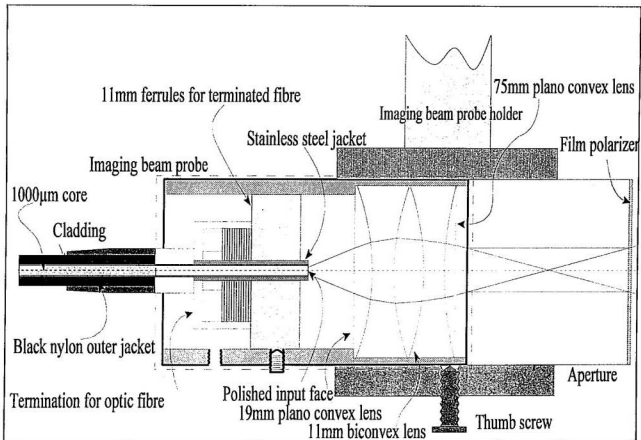


Figure 10 The Imaging Fibre Optic Probe

incident on the interface at less than critical angle. Only rays within the acceptance cone defined by a would be guided through the fibre by repeated reflections at the interface. A popular measure of the solid angle of the acceptance cone a is called the *Numerical Aperture* (NA), it is defined as follows:

$$NA = \sin a = \sqrt{n_1^2 - n_2^2} . \quad (12)$$

The relative difference in the refractive indices between the core and the cladding determines the acceptance cone angle. As light propagates through the fibre, it will experience losses in its intensity, these losses are due to absorption and scattering from the core material. Losses are experienced even as light enters and exits the fibre, since reflections occur at these surfaces. These losses are measured by the transmittance of the optical fibre, which is dependent on the wavelength, length of fibre, material used in the core of the fibre and the reflectivity of the end surfaces. The higher the transmittance, the lower are the losses. The transmittance - length relationship for constant wavelength is approximately as follows,

$$T = P(1 - R)^2 e^{-\alpha L} , \quad (13)$$

where P is the packing fraction (1 for single fibres and liquid light guides), R is the reflection loss, α is the absorption coefficient and L is the length of the average light path through the fibre[31]. Figure 11 shows a plot of the transmittance versus the wavelength of light for the single optical fibre used in our experiment, as reproduced from the Oriel Corporation catalog vol. II, page 4-6. The transmittance curve shows that the transmittance at 514.5 nm is about 95%.

The characteristic of the emergent cone of light from the fibre depends both on the properties of the optical fibre and the launching conditions of the entry cone of light into the fibre. For a long fibre (greater than 1 metre), the fibre properties dominate the characteristics of the emergent cone. This applies to the characteristic of the emergent cone of our optical fibre too. For a short fibre (shorter than 1 metre), the launching conditions dominate the

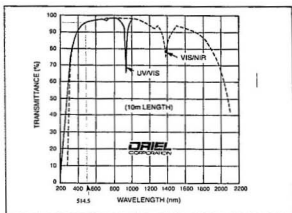


Figure 11 The transmittance curve for a 10m long fused silica single fibre.

emergent cone properties. Another characteristic of the emergent cone pertains to the angle at which the emergent cone exits the fibre, it would exit it at the angle specified by the NA , regardless of the angle at which the cone of light enters the fibre. This is due primarily to the fact that the coherent properties of the optical field in the entry cone cannot be related to the coherence properties of the optical field in the emergent cone, i.e optical fibres are incoherent[32].

Even though light may enter the optical fibre with its intensity evenly distributed about its cone, the light cone that exits the fibre very often does not have an even distribution of intensity. We can look at the intensity distribution in the emergent cone by simply placing a piece of cardboard about 20 cm from the output end of the fibre. Rather than seeing an evenly distributed circle of light, we would see symmetrical light patterns like those shown in Appendix B. These are manifestations of the so called 'propagative modes' of optical fibre. This means that although light enters the fibre at a continuous distribution of angles, it can only propagate through the fibre at certain angles. This is because of interference effects arising from the coherent nature of laser light. These propagative modes will be discussed in detail in Appendix B. The single optical fibre that we used in our experiment is a single multimode fibre from Oriel, it has a core diameter of 1000 μm . Optical fibres that

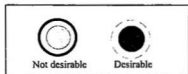


Figure 12 Some of the modes seen from our optical fibre.

allow only one mode to exist in the fibre are called single mode (monomode) fibres. Their core diameters range from 5 to 10 μm , they are generally used for communication purposes. The number and the types of modes present in an optical fibre depends not just on the dimension of the fibre, but also on factors like launching conditions, stress in the fibre and bending of the fibre. Launching conditions include factors like the angle of the entry cone of light (preferable to have it at the focal point or the image distance of the input lenses) and the amount of core surface it occupies on entry into the fibre. The above conditions that affect the mode distributions will have to be carefully optimized if a desirable output from the fibre is to be achieved. Some of the modes seen from our fibre are shown in Figure 12. An unoptimized fibre may produce modes that have most of their light distributed to the ring of the mode pattern whereas an optimized fibre would distribute most of the light evenly at the central circle, producing only a very faint ring around it. This is desirable as the diaphragm in the collection optics collects only light from the central part of the emergent cone. Some of the other mode characteristics of an unoptimized fibre may show up as time dependent intensity fluctuation, streaks of lines across the mode pattern or a combination of the above mentioned characteristics.

The solid angle of the cone of light that enters the optical fibre is determined by the set of complex lens and the aperture attachment in the imaging fibre optic probe. The aperture attachments are solid cylindrical brass pieces that are 15.7 mm in diameter and 12.7 mm in length with a hole bored axially into them. The hole may be of 6.35 mm or 1.59 mm in diameter. The aperture attachment sits partially and freely in the imaging fibre optic probe holder with the imaging beam probe. Choosing different hole sizes would allow scattering of different angular ranges to be collected. From now onwards, I shall refer to the hole in the cylindrical brass piece as the "collecting aperture" and the cylindrical brass piece as the

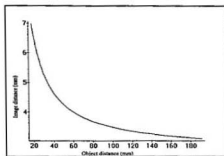


Figure 13 Distances of images form by the imaging beam probe for objects at various distances.

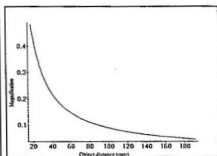


Figure 14 Magnification of images for various object distances.

“aperture attachment”. As the solid angle of the light cone entering the probe is limited by the aperture, light that is scattered or reflected from other surfaces in the gas cell that is outside this cone would not be collected, thus reducing noise. Since the angle of a ray that enters the optical fibre is determined by the angle at which this ray that enters the imaging fibre optic probe, we can match the input cone into the optical fibre to its numerical aperture by choosing an appropriate aperture size. We have also an aperture that is 25.4 mm in length and 1.59 mm in diameter. This as mentioned earlier in this chapter, is used for determining the angle of scattered light that is collected by the probe.

If the direction of polarization of the scattered light needs to be known, aperture attachments with polarizer film are used. The polarizer film is attached to the front end of the aperture attachment as shown in Figure 10. Since the aperture is free to move in the imaging fibre optic probe holder, rotating this polarizer aperture would allow us to vary the intensity of the scattered light collected and to subsequently determine its polarization direction.

The complex lens system in the imaging fibre optic probe would image a segment of the main laser beam in the cell onto the optical fibre input surface. The image will be real and diminished. Figure 13 shows a plot of the image distance for various object distances calculated from the thin lens equation applied to the series lens arrangement shown in Figure 10. Figure 14 shows the magnification of the images for different object distances. The

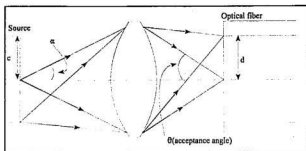


Figure 15 Coupling of light rays at maximum efficiency

lenses are 6.35 mm apart. In order that all the light from a source is coupled to the optical fibre at maximum efficiency, we must ensure that all rays from the source enter the fibre at angles equal to or less than the angle specified by the numerical aperture [33]. In order to achieve this, a lens or an image-forming system, that focuses the image of the source onto the input end of the fibre will be needed as the coupler. An approximate method of determining the focal length of the imaging system and the source size for maximum coupling to a fibre of a particular diameter is shown in Figure 15. The magnification of the imaging lens is α/θ , if the size of the source c is equal to $d\theta/\alpha$, where $2d$ is the core diameter, all the light from the source will be coupled to the fibre. Therefore, for a given magnification α/θ , any source with size less than $c = d\theta/\alpha$ would have all its rays coupled into a fibre of radius d . If the size of the source is larger than c , we would need to reduce the magnification so as to completely image the source into the fibre core. Reducing the magnification would require decreasing the image distance and increasing the object distance. But in doing so, we would increase the angles at which rays enter the fibre, thus losing rays that enter the fibre at angles larger than those specify by the numerical aperture.

The imaging fibre optic probe is mounted on the fibre optic probe mount via an imaging fibre optic probe holder, as shown in Figure 8. Since the holder is held to the fibre optics mount by a thumb screw, it can freely rotate about its axis when the thumb screw is loosened. The fibre optics probe mount is attached to a Edmund Scientific x - y - z low profile micropositioner with a metric micrometer drive. The imaging fibre optics probe can therefore be linearly positioned along the xyz axis and angularly positioned in the xz

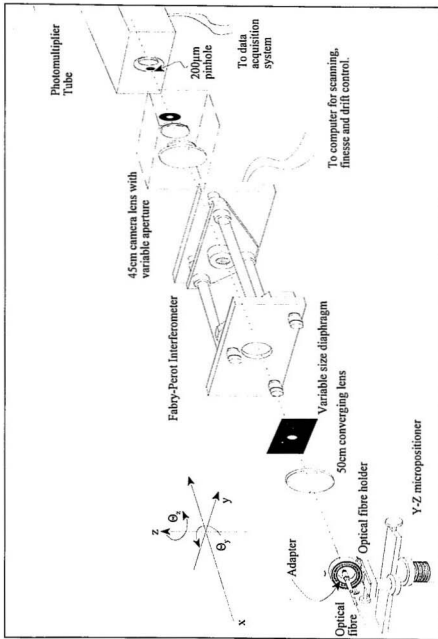


Figure 16 Output section of Collection optics

plane. The scattered light is channeled to the output section of the collection optics by means of an optical fibre. The optical fibre is a 1000 μm diameter single fibre¹ from Oriol. One end of this optical fibre is attached to the imaging beam probe and the other end leads to an optical fibre holder in the output section of the collection optics. This completes our discussion of the input end of the collection optics.

2.5.2 Output End

The setup for this section is shown in Figure 16. The optical fibre is attached to the optical fibre holder by means of an adapter, and the holder mounts on to a xz micropositioner. The optical fibre holder itself allows limited θ_y (pitch) and θ_z (yaw) adjustment so that, together with the micropositioner, the output end of the optical fibre can be positioned both linearly in the x, z axis and angularly in the θ_y and θ_z direction.

Scattered light leaves the optical fibre at a position that is located at the focal point of a collimating convex lens. The function of this lens is to produce a beam of collimated light whose direction of propagation is perpendicular to the plane mirrors inside the Fabry-Perot interferometer. The focal length of this convex lens is 50 cm. The variable size diaphragm after the collimating lens serves to control the amount of light and the size of light beam going into the Fabry-Perot interferometer. By doing so, it limits only rays from the paraxial region into the Fabry-Perot interferometer. Also, moving the diaphragm in the y, z direction would allow us to choose a path through the Fabry-Perot at the flattest possible regions of the mirrors. Since mirrors, in general are not equally flat throughout their surfaces, it is important that the light beam select the flattest parts of the mirrors so that they can maintain as high a parallelism as possible with each other. This would allow us to optimize the figure (variation in the surface flatness) finesse of the interferometer. If d is the mirror (plate) separation and Δd is the variation of the plate separation due to variations in surface flatness given by $\Delta d = \frac{\lambda}{M}$, then the figure finesse is given by $F_f = \frac{M}{2}$.

To analyze the spectrum of scattered light, we use a Burleigh piezo-electrically scanned Fabry-Perot interferometer. The Fabry-Perot interferometer is essentially made up of 2 highly parallel flat mirror plates facing each other and separated by a distance d . If an

¹Not to be confused with single mode fibre. This single fibre is a multimode fibre.

extended source (i.e source with diameters of at least a few mm) is used to send an incident beam of light into the Fabry-Perot interferometer, a concentric ring pattern will be seen at the output of the interferometer. Bright circular fringes signify constructive interference and dark fringes signify destructive interference. As we change the distance of the plate separation d , the optical path lengths of the interfering rays change and rays that had interfered constructively before may now interfere destructively. Where we had seen bright fringes before, we may now see dark fringes and vice versa. If we move the plates continuously and gradually closer together, we will see the concentric ring pattern collapsing into the middle. For a beam of light from a very small source (less than 1 mm in diameter), rather than seeing concentric ring pattern collapsing, we would see a single spot of light blinking as the plate separation is continuously changed. This spot of light does not disappear instantaneously, it shrinks before disappearing and then reappears again.

If our extended source consists of not just one frequency of light but a range of frequencies, we would in addition to seeing bright concentric rings (for strongest frequencies) also see weaker intensity concentric rings (from the weaker frequencies) between the bright ones. This is because the different frequencies require different optical path lengths for constructive and destructive interference. For a very small source, we would see weaker spots appearing in between the appearances of the brighter ones as the plate separation is changed. From this, we can see that the Fabry-Perot interferometer can be used as a highly discriminating optical filter. Selecting different plate separations would allow us to selectively change the frequency of light that gets through the interferometer.

In our Fabry-Perot interferometer setup, a very small extended source (output from optical fibre) is used and a set of piezoelectric drivers changes the plate separation as the Data Acquisition System (DAS) scans the scattered light spectrum. The total distance that the piezoelectric drivers move in one scan is separated into 640 steps. Each of these steps corresponds to one channel in the DAS. After each step, the piezoelectric drivers will stop for a specified amount of time to allow the DAS to acquire data. This is called the channel dwell time (specified in μsec). A larger dwell time may be needed if the signals are weak and a shorter one may be chosen if the signals are strong. Since each channel is associated with a different plate separation, they can therefore be calibrated to the frequency (or wavelength)

of light that gets through the Fabry-Perot interferometer. Calibration is done by first calculating the free spectral range (FSR) of the Fabry-Perot from the plate separation using the formula $FSR = \frac{c}{2nd}$, for air n is 1 and c is the speed of light. Dividing the FSR by the number of channels in one FSR would give us the frequency shift for one channel, e.g a plate separation of 110 mm would give a FSR of 1.36 GHz. For 256 channels per FSR, one channel would therefore be equivalent to 5.31 MHz.

Optimization of the Fabry-Perot interferometer is done through the drift and finesse controls in the DAS. The drift control in the DAS automatically locks on to the frequency of the reference beam² and corrects for any axial drift of the interferometer cavity or frequency drift from the laser. The finesse control optimizes the figure finesse of the Fabry-Perot interferometer by actively tilting the piezoelectric mirror mount so as to maintain minimum variation in plate separations across the beam diameter. A variation in the plate separation across the beam diameter gives rise to a phase variation in the transmitted rays, resulting in a loss of the figure finesse, just as in the variation of the mirror's surface flatness. The optimization is initiated when the DAS registers an intensity drop in the reference beam. This is done by comparing the intensity in the current scan from the previous scan. If the intensity drop is larger than a specified value, the piezoelectric drivers mounted mirror would be tilted through various angles to attempt to regain the intensity loss. Once the intensity rises again, the optimization process will stop. The finesse control also helps in compensating for any loss in the figure finesse due to minute variations in the solid angle of the emergent cone. These angular variations in the emergent cone are generally due to thermal or mechanical (vibrations) effects in the collection optics. Since the reference beam follows the same propagation path as the scattered light, optimizing on the reference beam would consequently yield optimization for the scattered light. The mirrors and piezoelectric drivers are mounted on a Super-Invar framework. Because of its zero thermal coefficient of expansion near room temperature, the Super-Invar material in the framework would help minimize frequency drift in the Fabry-Perot interferometer. A temperature controller for the Fabry-Perot interferometer is available if temperature fluctuation in the

²The Rayleigh line from the scattered light is too weak to be used for this purpose.

environment surrounding the interferometer affects its operations.

A 45 cm camera lens focuses the collimated beam of light from the Fabry-Perot to a 200 μ m pinhole before it reaches the Photomultiplier Tube (PMT). The pinhole is placed at the focal point of the camera lens. The purpose of the pinhole is to limit the angular range of the rays from the Fabry-Perot to the PMT, which helps to improve on the wavelength resolution of the Fabry-Perot. A measure of this effect is called the pinhole finesse defined as $F_p = (4\lambda_0 f^2)/(a^2 d)$, where f is the focal length of the camera lens, λ_0 is the light wavelength and a the diameter of the pinhole [34]. The net finesse of the Fabry-Perot interferometer is therefore a combination of the reflectivity finesse F_r , the figure finesse F_f and the pinhole finesse F_p . The net (instrument) finesse F_i is given as follows:

$$\frac{1}{F_i^2} = \frac{1}{F_r^2} + \frac{1}{F_p^2} + \frac{1}{F_f^2} \quad (14)$$

Other than the single fused silica fibre used for scattered light collection, I have also found it to be useful to use a larger diameter liquid³ light guide to perform coarse alignment to the Fabry-Perot interferometer. The light guide is 3 mm in diameter and has a numerical aperture of 0.47 (28°), it also possesses good transmittance for wavelengths from 250 nm to 700 nm. Because of these characteristics, it can transmit a large quantity of light from the laser to the position where the output end of the single fibre sits. This is done by removing the adapter (Figure 16) with single fibre from the optical fibre holder and replacing it with an identical adapter with a liquid light guide. Aligning to this extended source would narrow down considerably the range of adjustments required for the alignment of the single fibre's output. Using this bright 514.5nm wavelength extended source, we are able to align the Fabry-Perot interferometer manually by looking at the behaviour of the light beam coming out of the interferometer, while it is being scanned. When properly aligned⁴, we should be able to see an image of distinct collapsing rings at the back pinhole position. After this is

³Essentially a optical fibre with a large core filled with a non-toxic anaerobic liquid.

⁴The plates are still not parallel to each other at this stage, but they are parallel enough to create an interference pattern centred at the pinhole.

done, the single fibre with its adapter will be put back into the optical fibre holder and finer adjustments can be made thereafter to the interferometer and its optics. These fine adjustments are usually made while the DAS acquires and displays a spectrum of the reference beam. This method of coarse adjustment followed by finer adjustment is especially useful when the plate separation in the interferometer is changed. This often results in a gross misalignment of the interferometer.

The DAS used in our experiment is a microcomputer based data acquisition system, design and developed by Orlando Vazquez in this laboratory. The software that controls this system can be easily modified or upgraded if the need arises. The microcomputer used in this system is an IBM compatible 80386DX PC, it collects data from the PMT through a data acquisition card and controls the power amplifier to the piezoelectric elements in the Fabry-Perot through Digital to Analog Converters on an Input/Output Card. The PMT is water cooled to maintain low dark counts. Electrical pulses generated from photoelectric effect in the PMT are sent through an amplifier/discriminator and a pulse inverter before they reach the data acquisition card in the microcomputer. This concludes our discussion of the optical setup in our experiment.

2.6 The Gas Scattering Cell

The gas scattering cell is the central component of our experimental setup. It is the place where the gas to be studied is housed, where the gas can be subjected to a temperature gradient and where light scattering occurs. The gas scattering cell is designed and constructed by Dr. M.J. Clouter and assembled by me.

The design and the dimensions of the gas cell are shown in Figure 17. It is essentially made up of a cylindrical stainless steel tubular body with copper plate covers at the top and bottom. The good thermal conductivity of the copper plate makes it easy for heat to flow into and out of the cell. The bottom copper plate acts as a good heat sink, it is cooled by running water through copper tubings attached to it. The water is cooled by running it through a Lauda constant temperature bath and refrigerated circulator, model K-2/R. The top copper plate acts as a heat source for the temperature gradient, the heating here is provided by a simple heater ribbon. There is no temperature control for the heat source and temperature adjustments is made by input voltage adjustments through a Variac. Temperature gradients

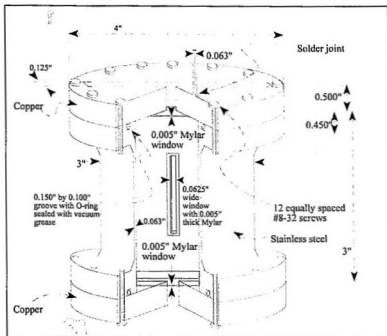


Figure 17 Gas scattering cell dimensions. The gas cell has front and back Mylar windows.

created by the heat source and sink can be maintained for a period of up to 3 to 5 hours.

Since stainless steel has low thermal conductivity and high mechanical strength, it allows for the construction of a cell with thin walls (1.6mm or 0.063 inch) and yet with the ability to withstand high pressures. The cell walls, being of low thermal conductivity, allow us to reduce thermal conduction along the stainless steel tube length to a low level so as to permit maintenance of the required temperature gradients with modest power dissipation in the top heater. To minimize wall effects, we want the walls to be far away from the centre of the cell. But this requires a larger volume and thus thicker walls to maintain mechanical stability. The present design of the gas cell walls seeks a compromise between the need for low thermal conduction along the length of the cell and the need to minimize wall effects while at the same time keeping the cell to a reasonable size. The geometry of the cell

provides a cylindrically symmetric volume of gas that is 76.2 mm (3.00 inch) in diameter and 76.2 mm (3.00 inch) in height. This is to ensure that minimum wall effects are present at the centre of the cell, where light scattering is to take place. The gas is channeled into the cell through a 1.6 mm (0.063 inch) diameter stainless steel capillary tube. The sulphur hexafluoride gas used in this experiment is supplied by Matheson Gas Products and it is 99.8 % pure.

All the cell windows are made from 0.1 mm (0.005 inch) thick Mylar. Its transparency and strength make Mylar a good choice as material for the windows and in the present arrangement, easily withstood pressures of up to 1.96 MPa (270 psig)⁵. Since it is very thin, the top and bottom Mylar windows allow good heat transfer from the heat source to the gas and from the gas to the heat sink. In order to look at scattering close to the bottom of the cell, we need to block off scattering from the bottom window by inserting a mask into the slot at the bottom copper plate. The side windows allow us to look at the path of the main beam and the amount of reflections and scattering that occur inside the cell. Significant amounts of reflections and scattering of the main beam do occur at the bottom window, especially if the main beam is not incident onto it perpendicularly. These stray light rays may be deflected from the walls of the cell and into the imaging fibre optic probe, even though the walls are painted black.

⁵ 14.7 psia = 14.7 + 0.0 psig = 0.101 MPa , 1 MPa = 1x 10⁶ Pa .

Chapter 3

Simulation Of Scattered Ray Paths In SF₆ Gas With A Density Gradient

3.1 Introduction

In any light scattering experiment, observation of scattered light originating from a point source at one scattering angle is often highly desirable but in practice not attainable. In any practical light scattering experiment, scattered light from a range of scattering angles originating from a region of scattering sites is observed through the collection optics in order to attain an acceptable signal level. In the present experiment, the scattered light experiences many changes in refractive index as it propagates through and out of the gas cell. The cone of scattered light that would have been observed if the propagation path of the light rays had not experienced any refractive index change before it enters the probe, would consequently be modified in our case. To find out the range of scattering angles and sites that are being observed, a computer simulation of the ray paths propagating through the density gradient to the optical fibre would have to be used. The angles at which the scattered rays enter the optical fibre can also be found from this simulation, and this would allow us to determine if our scattered light entry cone into the fibre is within the acceptance cone of the optical fibre.

In order to perform this computer simulation, we would first need to simulate the steady state distribution of some of the thermodynamic variables along the height of the cell, this includes temperature, thermoconductivity and density. From these simulation, we would also be able obtain an estimate of the temperature and sound velocity gradients at different heights in the cell. From the density distribution, we would be able to find the refractive index distribution at steady state. These distributions are obtained from a simple 2

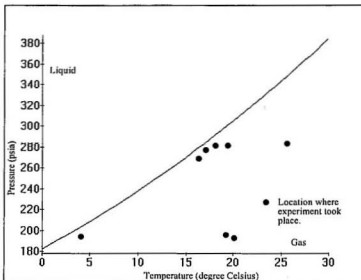


Figure 18 Vapour Pressure curve of SF_6

dimensional non-convective heat flow model of SF_6 gas subjected to a temperature gradient in the cell. After the refractive index distribution is obtained, we can perform a ray tracing of all the possible scattered ray paths from all possible scattering angles and sites. From all these ray paths, we would choose only those rays that were able to pass through the collecting aperture for further analysis.

To begin our discussion on the computer simulation of thermodynamic variable distributions in the cell, we will first look at some of the thermodynamic properties of SF_6 and the equations that are used to describe them.

3.2 The Sulphur Hexafluoride Gas

Most of the physical properties of SF_6 [35] are shown in Appendix A. The vapour pressure curve of SF_6 from $-50^\circ C$ to $45.6^\circ C$ can be fitted to the following equation[35],

$$\log \frac{101.325}{14.696} P_{\text{mm}} = 0.87652594 - \frac{816.48995}{T} + 0.029287342T - 0.40107549 \times 10^{-4} T^2$$

$$+ 0.7142667 \frac{(319.802 - T)}{T} \log(319.802 - T) , \quad (15)$$

where T is in Kelvins. This vapour pressure curve is shown in Figure 18. The regions where some of our experiments took place, with respect to the vapour pressure curve, are also shown in Figure 18.

The equation of state for a nonideal gas may be represented by virial coefficients as follows [36],

$$\frac{PV}{nRT} = 1 + \frac{B(T)}{V} + \frac{C(T)}{V^2} + \dots = Z , \quad (16)$$

where Z is the compressibility factor and the second virial coefficient of SF₆ is given as follows [19],

$$B(T) = B_0 - \frac{A_0}{RT} - \frac{c}{T^3} , \quad (17)$$

where A₀ = 1.064 × 10⁶ (m³ mol⁻¹)² MPa, B₀ is 2 × 10⁻⁴ m³ mol⁻¹ and c = 1.24 × 10³ (mK)³ mol⁻¹. If only the second virial coefficient is used in equation (16), it is accurate to within 1% for densities less than 100 kg m⁻³ [19].

The relations between thermal conductivity and temperature for gaseous SF₆ can be expressed as follows [19],

$$K = 4.84 \times 10^{-5} T^{0.85} \left(1 + 3.35 e^{-\frac{T_r}{T}} \right) , \quad (18)$$

where T_1 is the triple point temperature. Equation (18) is only valid to within 5% in the temperature range of 230 K to 1000 K. It should be noted from equation (18), that the thermal conductivity does not depend on density.

The molecular weight of SF_6 is $146.07 \text{ g mol}^{-1}$, it is one of the heaviest gases known. It is colorless, odourless, tasteless. Since all the valence electrons of the sulphur atom are shared with those of the fluorine atom, SF_6 possesses high chemical stability. SF_6 is also a substance of excellent electrical characteristics: its high dielectric strength has made it one of the most commonly used electrical insulators, especially in the liquid state.

The computer simulation of a thermodynamic model of our experiment, to be presented in the following section, will be based on the preceding equations discussed and does not claim to accurately represent the experimental conditions. This model should be treated as the simplest non-ideal gas approximation to the actual conditions. It exhibits some of the qualitative features that are expected of the experiment and should be regarded only as an initial approach to the problem.

3.3 Computer simulation of the density distribution in a temperature gradient .

Since the cell has cylindrical geometry with no angular variations, we can assume that the 2 dimensional temperature profile is the same as that of a 3 dimensional one. The heat flow geometry is shown in Figure 19. The simulation procedure described in the following paragraphs is essentially that suggested by Dr. J.C. Lewis [37].

Assuming no convective flow, and neglecting wall effects, the steady state temperature distribution of the cell can be described by the following heat flow equation,

$$\nabla \cdot (K \nabla T) = 0 \quad , \quad (19)$$

where K is the thermal conductivity and T is the temperature. Since both of the above variables are a function of height only, they can be rewritten as

$$\frac{d}{dz} \left(K \frac{dT}{dz} \right) = 0 \quad . \quad (20)$$

Integrating this equation gives

$$T(z) = T_0 + A \int_0^z \frac{dz'}{K(z')} \quad , \quad (21)$$

where A is a constant that is found from the boundary conditions of $T(z)$.

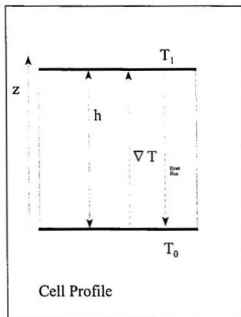


Figure 19 2-D nonconvective heat flow model.

From Equation (18), we know the relations between the thermal conductivity of SF₆ and temperature. If we have an expression of temperature as a function of z , we can substitute this expression into Equation (18) to get K as function of z . Substituting this expression of $K(z)$ into (21), would then allow us to find the temperature distribution along the height of the gas scattering cell. Since solving for $T(z)$ in (21) requires the substitution of $T(z)$ into this expression, an iteration process must be setup to repeatedly solve (21) until the solution converges. We can do this by starting off the iteration process by using a simple linear approximation for the temperature distribution as follows:

$$T(z) = T_0 + (T_1 - T_0) \frac{z}{h} \quad (22)$$

Next, we find K as a function of z from (22), then substituting $K(z)$ into (21) and solving that equation numerically yields a temperature distribution $T(z)$ that is of a higher approximation than the previous one. Repeating this process with the new $T(z)$ would give us another $T(z)$ that is of a still higher approximation. We continue repeating this process until $T(z)$ converges. The program that I have written to perform the above process converges to the 3rd significant figure after 5 iterations and to the 6th significant figure after 15 iterations.

After finding a satisfactory solution to $T(z)$, we will next proceed to find the density distribution along z in the cell. We can do this by first looking for a relation between density and temperature for SF₆. The density at a given pressure and temperature can be found from a virial equation (16) that is corrected to the second coefficient as follows,

$$\frac{PV}{RT(1 + \frac{B(T)}{V})} = \frac{m}{M} \quad (23)$$

where m is the mass of gas and M is the molecular weight of SF₆. Assuming constant volume, equation (23) would yield the following density equation for a unit volume:

$$\frac{PM}{RT(1 + B(T))} = \rho \quad (24)$$

$$\frac{PM}{RT+B_0RT-A_0-\frac{RC}{T^2}}=p \quad (25)$$

Alternatively, we can derive the following density relation from the Van der Waals equation,

$$\frac{M}{RT}(p+a)(1-b)=p \quad (26)$$

where a and b are constants that are functions of both the critical pressure and temperature. Comparing equations (25) and (26), we can see that (26) has an infinite discontinuity at $T = 0$ K whereas (25) has one at $T = 10.785$ K. Varying the constant parameters in the denominator of (25) would vary the position of its infinite discontinuity. Given that the density relation (25) is accurate only to 5 % for densities less than 100 kg m^{-3} [19], and becomes progressively less accurate at higher densities, no physical significance can be associated with this discontinuity. Here we assume the qualitative characteristics of the density variation above the discontinuity only as a first approximation at the problem.

Substituting a temperature distribution $T(z)$ and (17) into (25), would give us the density distribution $\rho(z)$. The known density of SF_6 at 25°C and 1 atmosphere is 6.08 kg m^{-3} , the density calculated from (25) for the same pressure is 5.95 kg m^{-3} , which gives a difference of about 2.1%. Assuming that mass is conserved after a temperature gradient is introduced into the system, we can perform an integration of the mass at different z , $m(z)$, from $z = 0$ to $z = h$ as follows to solve for the steady state pressure corresponding to the density distribution:

$$m = \int_0^h \rho(p, T(z)) S dz \quad (27)$$

where S is the horizontal cross-sectional area of cell. Starting from a known amount of gas m with an initial pressure p , we would expect the pressure to change as a temperature gradient is introduced into the system. Therefore the integral in (27) is not expected to give m from the initial value of p . A program loop is setup to progressively change the value of

pressure p until it satisfies equation (27). With the determination of this new pressure, we would have also had acquired a density distribution that satisfy (27). We will next set up a boundary condition for the density distribution that requires it to satisfies a known density at $z = 0$ (a density that is close to that of liquid SF_6). In order to satisfy this condition, T_0 in (21) and (22) will have to be repeatedly adjusted until a value of T_0 is found that would yield a density distribution with an appropriate density¹ (to within 50 kg m^{-3} of the specified value) at $z = 0$ and yet at the same time satisfy (27).

The refractive index of a gas is related to its density through the Lorentz - Lorenz relation [34] as follows:

$$\frac{(n^2-1)}{(n^2+2)} = L\rho ,$$

$$n = \sqrt{\frac{2L\rho+1}{1-L\rho}} . \quad (28)$$

The Lorentz-Lorenz coefficient for SF_6 was found to be $0.0783 \times 10^{-3} \text{ m}^3 \text{ kg}^{-1}$ [38]. Substituting the density distribution into (28) would allow us to easily find the refractive index distribution of SF_6 in the gas cell.

Figures 20 and 21 show the density distributions of SF_6 simulated from the above program for an initial pressure of 1.9 MPa (276.5 psia, 261.8 psig), the steady state pressure is 1.4 MPa . The temperature at the top is 300 K and at the bottom is 24 K. The simulated temperature at the bottom of the cell is obviously not realistic and very far away from the actual temperature at the bottom plate of the cell. The density distribution in Figure 20 shows that the density at the bottom approaches that of liquid. This is expected when working with

¹ The correct densities at $z = 0$ and $z = h$ is more important to us than the correct temperatures at these points since the densities affect the refractive indices directly.

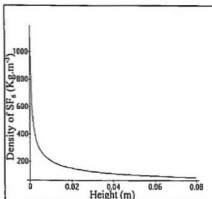


Figure 20 Distribution of densities of SF_6 along the height of cell

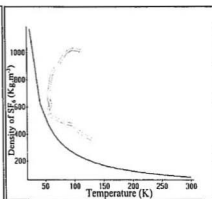


Figure 21 Density of SF_6 as a function of temperature.

a gas that is closed to the vapour pressure curve. The density at the bottom of the cell was calculated to be 1172 kg m^{-3} , which is close to that of liquid SF_6 (1336 kg m^{-3} [35]). At the top of the cell, we calculated the density of SF_6 to be 84.9 kg m^{-3} . This is very close to that of 84.3 kg m^{-3} for a SF_6 gas held a temperature and pressure of 298 K and 1.4 MPa respectively. Although the calculated vapour pressure curve (Figure 18) indicates that the density should increase rapidly as temperature approaches 277 K for a constant pressure of about 1.4 MPa (204 psia), this did not happen in our computer simulation. The rapid density increase only happened at a temperature of about 24 K in our simulation. This is probably because of the virial equation that we had used is only corrected to the second virial coefficient, which is good for a gas of moderate density, up to 100 kg m^{-3} . For a higher density gas, such as those that is observed when a gas is brought closed to the vapour pressure curve, the third or higher virial coefficients would be required. Furthermore, the density distribution was derived from a lack of information about the density dependence of the thermal conductivity. Nevertheless, since we were able to obtain a realistic representation of the densities of SF_6 at the top and bottom of the cell, we assume that the simulated density distribution over the remainder of the cell to be a reasonable first approximation. It

² Based on a density of 6.08 kg m^{-3} at a temperature of 25°C and a pressure of 1 atmosphere.

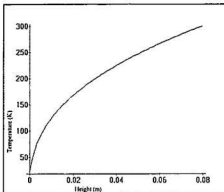


Figure 22 Distribution of temperatures along the height of cell

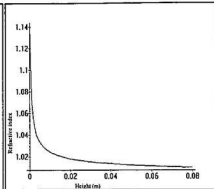


Figure 23 Distribution of refractive indices along height of cell

should also be noted that the nonlinearity of the density distribution is due primarily to the nonlinearity of the temperature gradient simulated for a set of temperature-density boundary condition. Therefore, even though the thermal coefficient of expansion of the gas remains relatively constant in the simulation, a large temperature gradient would result in a large density gradient. We will therefore use this density distribution to calculate the ray paths of the scattered light in the gas cell. This ray tracing program will be discussed in the next section of this chapter.

The Figures 22 and 23 show the simulation for the temperature vs height and refractive index vs height distribution of SF_6 in the gas scattering cell.

3.4 Ray tracing through the density gradient and the imaging fibre optic probe

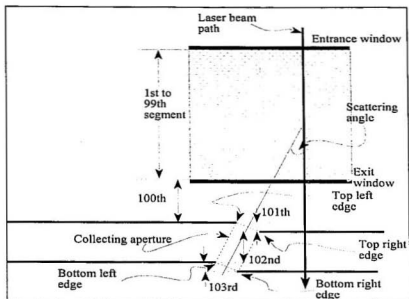


Figure 24 Axial cross sectional geometry of gas scattering cell and aperture.

In this section, we will trace the scattered light through the density gradient, into the aperture, then through the lenses in the imaging fibre optic probe and finally to the optical fibre.

3.4.1 Raytracing through the density gradient

In this program, I have divided the volume of gas into 100 layers. The refractive index of each layer (0.79mm high) of gas was determined from the previous density gradient simulation program. Scattered rays paths from sites starting from the entrance window going all the way down to the exit window will be analyzed. The sites are 0.79 mm apart along the path of the laser beam. From each site, scattered rays from scattering angles of 5° to 89° will be analyzed in incremental steps of 0.5°. The paths available to the emerging rays were determined by an aperture 1.59 mm in diameter and 12.7 mm in length, whose axis was oriented at 22° to the laser beam. Reflections at the inner surface of the aperture attachment

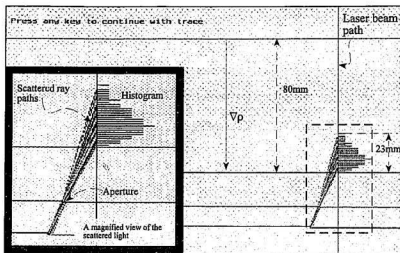


Figure 25 Scattered ray paths through a density gradient, as seen from output of simulation program. Inset shows a magnified view of the ray paths. The histogram on the right of the ray paths shows their relative frequency of occurrence.

were ignored so that the axial cross-section of its inner surface represented in Figure 24 has the effect as two apertures in series, which will thereafter be referred to as the “collecting aperture”. A ray starting off from a scattering site and ending at the collecting aperture may have up to 103 segments, depending on where the scattering site is located. The 1st to 99th segments define the ray path through the density gradient in the gas. The 100th to 103rd segments define the ray path through air from the exit window of the cell to the aperture. These are shown in Figure 24. The ray path will be calculated and the coordinates of the ray compared to the coordinates of the aperture, if the ray path falls within the aperture then that ray will be plotted out. This program will start by first tracing a scattered ray through 103 different layers from a scattering angle of 5° at a scattering site located at the entrance window. It will then increase the scattering angle by 0.5° and the next scattered ray will be traced through the 103 layers again. It will continue to do this until it reaches 89° , after which the scattering site position will be decremented by 0.79 mm along the path of the laser and scattered ray paths from scattering angles of 5° to 89° will again be traced. By the time the last scattering site is analyzed, all probably scattered ray paths (except for reflected rays)

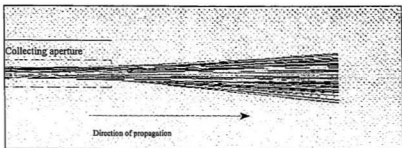


Figure 26 A magnified view of scattered ray paths through aperture.

from SF_6 that are on the left side of the laser beam would have been analyzed for their possibility of entry into the aperture. An actual output from this program is shown in Figure 25. In this simulation, the aperture is position at 22° to the laser beam path and the top left edge of the collecting aperture is 11.9 mm away from the laser beam. The relative amount of scattered rays that are able to get through the aperture from a scattering site is indicated by a horizontal line left of the scattering site. A longer line indicates more scattered rays from this site were able to get through the aperture. From these lines, we get an intensity distribution of scattered light from the scattering sites. Figure 25 shows that this distribution is not symmetric. This is probably due to the fact that the aperture is not perpendicular to the laser beam. For an aperture of the size and at the position specified earlier, the region of scattering sites observed by the collection optics consists of a segment along the laser beam path that is about 23mm in length.

The next trace in this program will show a magnified view of the rays going through the collecting aperture and the paths that these rays will take to propagate to a position that is 198.5 mm away along the optic axis from the entrance of aperture. The output of this program is shown in Figure 26. There will be no optical elements along their paths. We see a cumulative effect from the rays that show a beam of light confined to propagate along the collecting aperture and after that, diverges as it should. This can be served as a check to the accuracy of our ray tracing through the system; rays that don't get from the entrance to the exit of the aperture would not be plotted. The next trace will be a further development of this trace, which will involve tracing the ray paths through the aperture and through 3 lenses

in series, i.e we will trace the ray paths through the entrance optics of the imaging fibre optic probe. The scale for the first trace (Figure 25) is 32 pixels to 12.7 mm(0.5 inch) or 1 pixel to 0.397 mm. In the following trace (Figure 26), the scale is magnified 5 times and it is 160 pixels to 12.7 mm.

3.4.2 Ray tracing [39] through the imaging fibre optic probe

We start the discussion of ray tracing through a set of lenses by first considering a

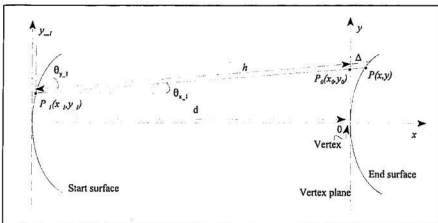


Figure 27 Transfer function coordinates

simple case of ray propagation from one point on a convex surface to another convex surface, as shown in Figure 27 . Our aim here is to transform the starting coordinates $P_1(x_1, y_1)$ of the ray on the starting surface to another set of ending coordinates $P(x, y)$ that specify the end point of the ray in the end surface.

From the above figure, we can express the coordinates of the point of intersection between ray and vertex plane $P_0(x_0, y_0)$ as follows,

$$y_0 = y_{-1} + h \cos \theta_{y,1}$$

$$y_0 = y_{-1} + \frac{M}{L}(d-x_{-1}), \quad (29)$$

where $M = \cos\theta_{y_{-1}}$ and $L = \cos\theta_{x_{-1}}$, and $x_0 = 0$, i.e. vertex of end surface is the origin. Also, from the diagram we can see that $y = y_0 + M\Delta$ and $x = L\Delta$, where Δ is the length of the ray from $P_d(x_d, y_d)$ to $P(x, y)$.

The equation of a circle with radius R whose centre is shifted by $x = R$ can be expressed as follows,

$$x = \frac{c(x^2 + y^2)}{2}, \quad (30)$$

where $c = \frac{1}{R}$ is the curvature of the circle. We can rewrite (30) in terms of Δ as follows,

$$\Delta^2 c - \Delta 2(L - cy_0 M) + y_0^2 c = 0, \quad (31)$$

where equation (31) is quadratic in Δ , so Δ can be expressed as follows,

$$c\Delta = G \pm \sqrt{G^2 - cF}, \quad (32)$$

where $G = L - cy_0 M$ and $F = y_0^2 c$.

Since Δ is zero when $x_0 = y_0 = 0$, we must choose the negative value of the square root in (32). By multiplying both sides of (32) by $G + \sqrt{G^2 - cF}$, we get the following:

$$\Delta = \frac{F}{G + \sqrt{G^2 - cF}}. \quad (33)$$

From (33), we can express x and y in terms of x_{-1} and y_{-1} , thus allowing us to transform the coordinates of the starting point of ray to the coordinates of the end point of ray. I will call this the transfer function of the ray.

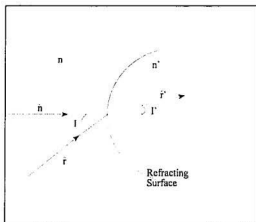


Figure 28 Vectors of incident and refracted ray

We will now proceed to discuss refraction at the interface of two media. Our aim is to find the new directional cosines of the ray after it has undergone refraction.

The vector form of Snell's law is expressed as follows:

$$n'(\hat{r}' \times \hat{n}) = n(\hat{r} \times \hat{n}) \quad (34)$$

The unit vectors are shown in Figure 28 . Equation (34) may be expanded to the following form:

$$n'\hat{r}' - n\hat{r} = \hat{n}(n'\cos I' - n\cos I) \quad (35)$$

The unit vectors can also be represented by their respective directional cosines,

$$\begin{aligned} \hat{r} &= L\hat{i} + M\hat{j} , \\ \hat{r}' &= L'\hat{i} + M'\hat{j} , \\ \hat{n} &= \alpha\hat{i} + \beta\hat{j} , \end{aligned}$$

where $\{L, M\}$, $\{L', M'\}$ and $\{\alpha, \beta\}$ are directional cosines of the incident ray, refracted ray and the normal vector to the surface, respectively. We can now express (35) in terms of the \hat{i}, \hat{j} unit vectors as follows,

$$(n'L' - nL)\hat{i} + (n'M' - nM)\hat{j} = \alpha k\hat{i} + \beta k\hat{j} \quad (36)$$

where k is $n'\cos I' - n\cos I$. Equation (36) implies the following:

$$n'L' - nL = \alpha k \quad , \quad n'M' - nM = \beta k \quad (37)$$

The unit normal vector (α, β) to the surface of a circle whose centre is shifted by the radius R in the x direction is given by $(1 - cx, -cy)$. Therefore we can rewrite (37) as follows:

$$L' = \frac{nL + k - c k x}{n'} \quad ,$$

$$M' = \frac{nM - c y k}{n'} \quad (38)$$

Also, since $\cos I = \hat{r} \cdot \hat{n}$, we can expand the dot product and get the following:

$$\cos I = \sqrt{G^2 - cF} \quad (39)$$

Furthermore, from Snell's law we get,

$$\cos I' = \frac{1}{n'} \sqrt{n'^2 - n^2(1 - \cos^2 I)} \quad (40)$$

Therefore k can be found from G and F through Equations (39) and (40). Substituting k into Equation (38), would allow us to find the refracted directional cosines L' and M' from the incident directional cosines L and M . This function that performs the directional cosines transformation will be called the refraction function.

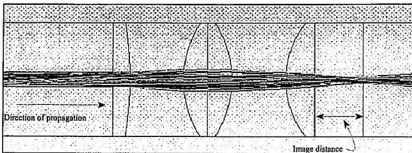


Figure 29 Scattered ray paths through fibre optic probe.

To trace a ray through a series of lenses would simply require the repeated application of the transfer function and refraction function to all the surfaces in the optical system. Our simulation of the 3 elements optical system used in the fibre optic probe consist of 8 surfaces rather than 6 because the simulated biconvex lens is actually two simulated plano-convex lens placed back to back. Altogether, there are 9 iterations in my program to simulate the ray going from the aperture entrance to the input end of the optical fibre.

Figure 29 shows the output of the program, it displays the paths of the rays through the lenses as calculated by the above program. The image distance, estimated from Figure 29, is about 5.6 ± 0.8 mm away from the last lens surface. The lowest value in this range of image distances estimated from the simulation differs from the calculated image distance of 4.4 mm, for an object distance³ of 44.5 mm, by 0.4 mm. This discrepancy is probably mainly due to the orientation of the collecting aperture with respect to the laser beam.

The range of angles at which the rays enter the optical fibre goes from -5.3° to 5.5° . This indicates a slight angular asymmetry in the cone of scattered light that enters the optical fibre. But nevertheless, these angles are well within the acceptance cone of the optical fibre, which goes from -12.7° to 12.7° . The range of scattering angles, as measured by their frequency shifts⁴, that were observed is shown in Figure 30. The range of frequency shifts

³ Base on an aperture angle of 22° and a aperture distance of 11.9 mm from the laser beam path

⁴ Calculated from a sound speed of 136 m.s^{-1} , mean refractive index of 1.05 and at a wavelength of 514.5 nm.

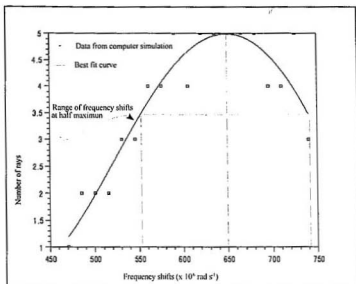


Figure 30 Relative intensity of scattered light entering optic fibre from different scattering angles.

(linewidth) observed at half the maximum intensity is estimated to be from $552 \times 10^6 \text{ rad s}^{-1}$ to $742 \times 10^6 \text{ rad s}^{-1}$, with the maximum number of scattered rays observed at a shift of about $650 \times 10^6 \text{ rad s}^{-1}$ (21.5°).

The scale in this Figure 29 is 160 pixels to 12.7 mm, which is 5 times larger than the scale used in the first ray tracing program.

Chapter 4

Experimental Results

4.1 Introduction

In this section, Brillouin spectra are presented for SF_6 gas in both equilibrium and nonequilibrium states. The Brillouin spectra for SF_6 gas in the equilibrium state serve to validate the working of our experimental setup, especially the optical fibre collection optics. These will be applied to finding the linewidths of the central (Rayleigh) and the Brillouin components of the scattered light. We will also use the spectra collected in the equilibrium state to observe the change in sound speed with pressure and compare it to some theoretical results from Equation 11 in Chapter 1. An extra set of unknown secondary peaks was observed together with the Brillouin components in the spectra. In order to determine the nature of these unknown secondary peaks, we had to design and carry out extra experiments that were not part of our original objective. Following this, I will look at 2 Brillouin spectra of SF_6 gas at nonequilibrium, observed at different pressures. All the observed scattering took place at sites that were close to the bottom of the gas cell and with a collecting aperture of size 1.59 mm in diameter and 12.7 mm in length.

4.2 Results

The Brillouin spectrum shown in Figure 31 was collected at a scattering angle of $22^\circ \pm 1^\circ$ with the gas pressure held at 1.28 MPa (171 psig) and the gas temperature at $20^\circ C$. The free spectral range (FSR) of the interferometer is 1.23 GHz with 256 channels separating the different orders of interference. Altogether, the Brillouin spectrum covers 2 free spectral range or 3 orders of interference. Each channel represents a frequency shift of 4.80 MHz. The finesse was about 26. Figure 32 shows an expanded view of the central component of the Brillouin spectrum. The linewidth of the Rayleigh line at half height was found to be

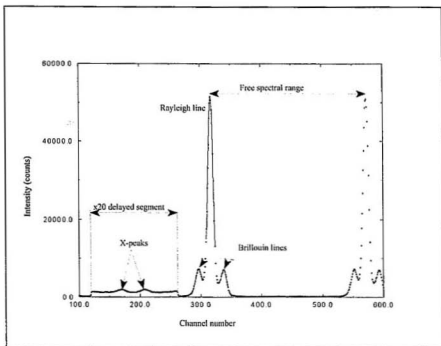


Figure 31 A Brillouin spectrum collected for SF_6 gas in an equilibrium state.

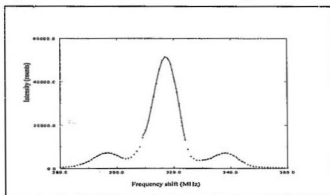


Figure 32 The Brillouin spectrum for one order of interference.

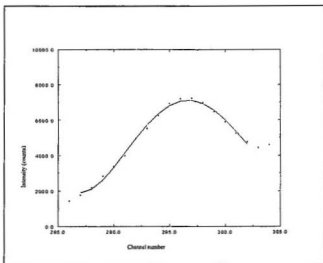


Figure 33 Linewidth of a Brillouin component.

50.5 ± 4.8 MHz. The frequency shift of the Brillouin line was measured to be 98.5 ± 4.8 MHz. This corresponds to a sound speed of 133 ± 6 m s⁻¹. From Figure 33, we can estimate the fullwidth of the Brillouin component at half height to be 54.0 ± 4.8 MHz. This would give us an angular frequency width $\delta\omega$ of $(332 \pm 60) \times 10^6$ rad s⁻¹, which is 82×10^6 rad s⁻¹ wider than the linewidth due to the finite collection cone as found by computer simulation.

The set of secondary peaks seen between the first and second order in Figure 31 is of an unknown nature, which I shall call X-peaks. The intensity of these peaks is weaker than the Brillouin components by about a factor of 100. There are no significant changes in the positions of these peaks when the scattering angle was varied from 22° to 36° . In order to determine the nature of the X-peaks, experiments had to be performed to ascertain if these signals are coming from the optical fibre, the gas cell or the SF₆ gas. This included using a 10 Å bandpass filter, centred at 514.5 nm, to remove any Raman components from the spectrum. The X-peaks could still be observed when the filter was used. The polarization of the X-peaks was found to be in the same direction as the Brillouin lines from the gas, thus the X-peaks were not depolarized.

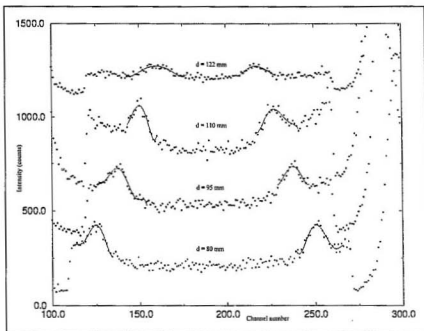


Figure 34 Changes in X-peaks position as the FSR is changed.

The next step in the quest into the origins of the X-peaks was to determine the order of interference these peaks belong to so that their frequency shifts can be found. The X-peak may belong to the order of interference associated with the Rayleigh line on either side of it or it may belong to an order that is more than one FSR away. Because of these complications, the FSR of the Fabry-Perot interferometer had to be varied so as to observe and measure the corresponding change in position of these peaks. From these changes in position, we can find out if the frequency shifts are greater or less than one FSR. If the shifts are less than one FSR, we would need to observe the direction in which a given X-peak moves as the FSR is changed so as to allow us to determine if it belongs to the order on its left or right. Figure 34 shows the relative change in the channel positions of the X-peaks for different free spectral ranges, determined by its plate separation d . The relation between the plate separation d and the frequency shift is as follows,

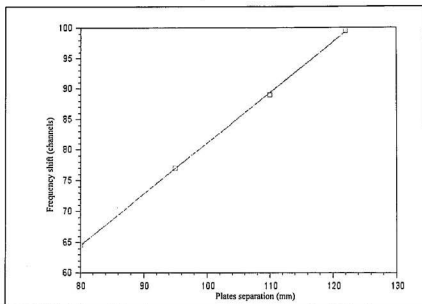


Figure 35 The number of channels used to represent a particular frequency shift is proportional to the plate separation in the Fabry-Perot interferometer.

$$d = \frac{(B+nN)c}{2N(f+nf_{fsr})}, \quad (41)$$

$$d = \frac{Bc}{2N(f+nf_{fsr})} + \frac{nNc}{2N(f+nf_{fsr})},$$

where B is the frequency shift in channels measured within one order, N is the number of channels per FSR, n is the number of order that the shift belongs to, c is the speed of light, f_{fsr} is the FSR and f is the frequency shift in Hz measured within one order. If f belongs to an order that is n FSR away, then the frequency shift would be $f + nf_{fsr}$. By plotting a graph of B vs d , we would get a slope of $\frac{2N(f+nf_{fsr})}{c}$. From Figure 35, we calculated the slope to be 0.83. From Figure 34, we can see that the X-peaks move away from each other and towards the Rayleigh line as the FSR is increased.

The behaviour of the X-peaks with changes in the pressure is shown in Figure 36. There is a noticeable increase in the frequency shift as the pressure is reduced. The signal to noise ratio gets lower as we get to about 1.01 Mpa (132 psig) and at 0.857 MPa (110 psig), the signal to noise ratio is so low that the X-peaks are hardly distinguishable. This contributes to the relatively large uncertainty in measuring its frequency shifts at low pressures.

As it was suspected that the X-peaks may originate in some form of secondary scattering process from a reflected laser light beam from inside the cell, a backscattering experiment was conducted to examine the behaviour of the backscattered Brillouin frequency shift for different pressures (at a temperature of about 19°C). This is done by reflecting the laser beam back into the cell with a concave mirror. At a backscattering angle of 158°(180°-22°), the backscatter frequency shift, seen from Figure 37 shows an increase in the frequency shifts as the pressure gets lower. The signal to noise ratio also gets lower as we go below 0.72 MPa (90 psig) and at 0.44 MPa (50 psig) the peaks are barely noticeable as they get even weaker and closer together. In Figure 38, we compare the changes in the frequency shifts of both the X-peaks and the backscatter peaks as we change the pressure.

The sound speed for SF₆ at different pressures can also be extracted from the above backscatter data. These are shown in Figure 39 with some theoretical data calculated by Equation (11) from Chapter 1; pressure is used instead of density in this case. The experimental data were fitted to a polynomial that is quadratic in the sound speed c .

Figure 40 and 41 compares the Brillouin spectra for SF₆ in the equilibrium and nonequilibrium states. The Brillouin spectra for Figure 40 were acquired at a pressure of 0.919 MPa (119 psig) at equilibrium and 0.891 MPa (115 psig) when at nonequilibrium. For the spectra in Figure 41, the pressure was at 1.38 MPa (186 psig) at equilibrium and 1.35 MPa (182 psig) at nonequilibrium. The temperature gradients for the Brillouin spectra in Figure 40 and 41 were at about 15.3 K cm⁻¹ and 18.9 K cm⁻¹ respectively. The values of the temperature gradients were based on the assumption that the simulated temperature profile is representative of the actual conditions in the gas cell. The temperature profile from the

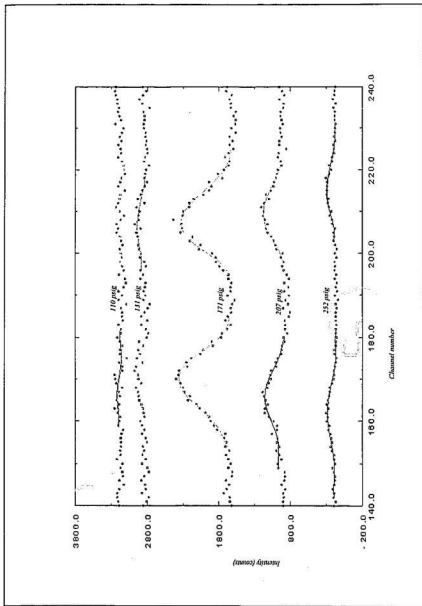


Figure 36 Changes in the positions of X-peaks as pressure is changed. Intensity comparisons are not meaningful.

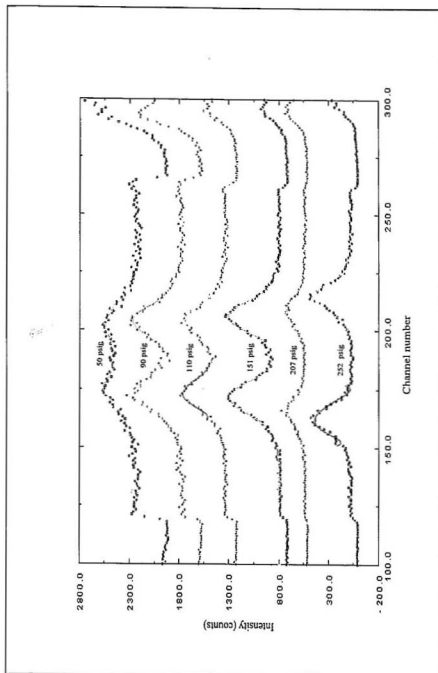


Figure 37 158° backscatter Brillouin peak position for different pressures. Intensity comparisons are not meaningful.

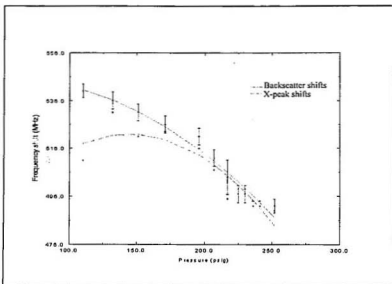


Figure 38 Comparison of the frequency shifts change between X-peaks and backscatter peaks as the pressure is changed.

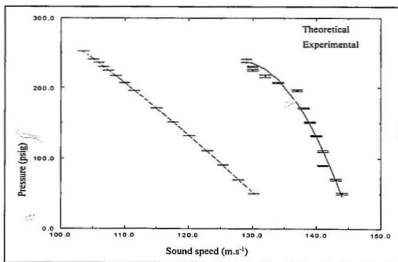


Figure 39 Sound speeds in gaseous SF_6 for different pressures.

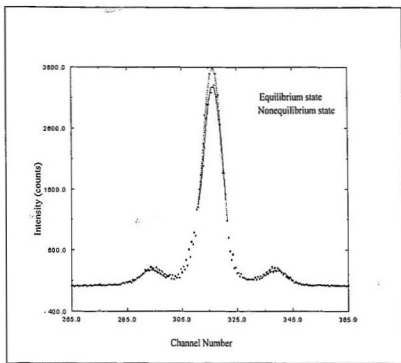


Figure 40 Changes in the SF₆ Brillouin spectrum intensity as it goes from a equilibrium to a nonequilibrium state. Pressure goes from 0.919 MPa (134 psia) to 0.891 MPa (130 psia).

simulation, shown in Figure 22 in Chapter 3, indicates that the temperature gradient at about 0.5 cm from the bottom of the cell is about 9 times greater than what it would have been if a linear temperature profile was assumed. The Brillouin spectra in Figure 41 were acquired at conditions that are closer to the vapour pressure curve than that of the other spectra, as shown in Figure 42. A larger density gradient was therefore expected to occur. The changes in the Rayleigh line intensity in going from an equilibrium state to a nonequilibrium state were $8.6 \pm 1.4\%$ and $15.5 \pm 1.4\%$ for the Brillouin spectra in Figures 40 and 41, respectively. The changes in the Brillouin component intensity in going from an equilibrium to a nonequilibrium state were $16.4 \pm 3.1\%$ and $16.7 \pm 3.3\%$ for the spectra in Figures 40 and 41, respectively. Also, there was observed to be a decrease in the Brillouin line shift in both

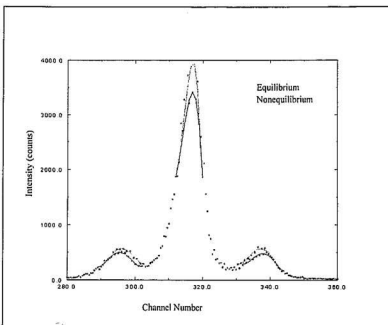


Figure 41 Changes in the SF₆ Brillouin spectrum intensity as it goes from an equilibrium to a nonequilibrium state. Pressure goes from 1.38 MPa (201 psia) to 1.35 MPa (197 psia).

cases when going from an equilibrium to a nonequilibrium state. This shift is about 4.8 ± 2.4 MHz. for both cases.

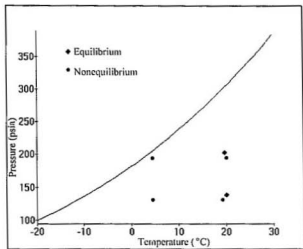


Figure 42 Positions of the experimental conditions with reference to the vapour pressure curve.

Chapter 5

Discussion

5.1 Discussion

We have demonstrated that the optical fibre technique used in this experiment was successful in acquiring a Brillouin spectrum of gaseous SF_6 , and was able to determine the sound speed of SF_6 to be $133 \pm 6 \text{ m s}^{-1}$ at a pressure of 1.28 MPa (171 psig) and a temperature of 20°C . This result agrees with the result from other experiment [35] of 136 m s^{-1} at a pressure of 0.1 MPa and a temperature of 25°C ; the speed of sound should be expected to be slightly lower than 136 m s^{-1} at higher pressures. The Brillouin component linewidth was measured to be $(332 \pm 60) \times 10^6 \text{ rad s}^{-1}$, which is $82 \times 10^6 \text{ rad s}^{-1}$ wider than the simulated line width of $190 \times 10^6 \text{ rad s}^{-1}$. The linewidth predicted from the simulations of Chapter 3 is therefore of the same order of magnitude as that of the measured one. One of the causes of the wider linewidth in the experimental Brillouin component may be due the fact that the cylindrical wall that makes up the aperture in the aperture attachment is reflective, in contrast to the nonreflective wall assume in the computer simulation. This would most probably direct rays from outside the solid angle defined by the nonreflecting aperture in the computer simulation into the imaging fibre optic probe. The Fabry-Perot interferometer and the collection optics will also contribute to the wider experimental Brillouin linewidth.

To determine the frequency shift of the X-peaks, we varied the plate separation d in the interferometer to observe changes in the number of channels required to specify a given peak position. The relation between the plate separation d and the number of channels required to represent the frequency shift was found to be linear with a coefficient of proportionality of 0.83. This corresponds to the value of 0.82 found from the slope of Equation (41) for an assumed frequency shift f of 478 MHz and $n = 0$. From this we can infer

that f is less than one FSR in magnitude. To find out which Rayleigh lines (the one on its left or right side) it belongs to, we need to look at the direction of change. As the FSR is increased, the number of channels used to specify a given peak position should decrease, therefore the peak will move towards its “parent” Rayleigh line. In other words, the slope of B versus d should be positive. We can now conclude from Figures 34 and 35 that the rightmost X-peak belongs to the same order as the Rayleigh line on the right and the leftmost X-peak belongs to the one on its left. We can therefore conclude that the frequency shift for the X-peak at a pressure of 1.78 MPa (245 psig) is thus measured to be 478 ± 4.8 MHz.

The frequency shifts of the X-peaks were found to increase as the pressure in the gas was decreased. This is similar to the changes in the frequency shift for the backscatter Brillouin component at 158° . Both types of peaks in the Brillouin spectra were found to be similar in magnitude and in the direction of change at pressures from 1.82 MPa (250 psig) to 1.13 MPa (150 psig). At pressures lower than this, their magnitude deviates. This is probably because of the difficulty in determining the maxima of the X-peaks at these pressures due to their low signal to noise ratio.

The direction of the polarization of the X-peaks, its frequency shift magnitude (small compared to frequency shifts from liquid and solids) and the similarity in its behaviour to backscatter Brillouin shifts as pressure varies, leads us to believe that the X-peaks originated from backscattering in the SF_6 gas by a beam of laser light reflected back up into the cell from the exit window as the main laser beam passes through it.

The sound speeds in SF_6 gas for various pressures were extracted from the data of the backscattering experiment performed previously. These data were fitted to a quadratic polynomial curve with the following coefficients:

$$p = -12462 + 198.1c - 0.773c^2 ,$$

which indicates a negative nonlinear term in the sound speed c . The theoretical relations [19] between pressure and sound speed is as follows,

$$p = \frac{M}{2B(T)\gamma} c^2 - \frac{RT}{2B(T)}, \quad (42)$$

where γ is the ratio of the specific heats, R is the universal gas constant, M is the molecular mass, p is the pressure, T is the temperature and $B(T)$ is the second virial coefficient. Since $B(T)$ is negative at 292 K, the theoretical relations contain also a negative nonlinear term in the sound speed. Comparing data from both theoretical calculations and experimental measurements shows that there is a stronger nonlinearity in the experimental values than the theoretical ones.

Our attempt to observe nonequilibrium effects in gaseous SF_6 is shown in Figures 40 and 41. An increase in the intensity of the Rayleigh line was observed. This increase may be due to optical effects created in the nonequilibrium gas. The change in the Rayleigh line intensity when the nonequilibrium condition was brought close to the vapour pressure curve was about twice as much as that when the nonequilibrium condition is further away. One of the reasons for this larger increase may be due to the higher densities and larger optical effects experienced in the former situation. Although there are theories and experiment [46] that attribute an increase in the Rayleigh line intensity to nonequilibrium effects, these effects were observed with systems that have a larger temperature gradient and smaller wavevector k than ours. To determine if any of the increase in the Rayleigh line intensity in our system is due to nonequilibrium effects would require further investigations.

There was observed to be an equal amount of increase in the intensity of the Brillouin components in both cases of about 16%. It seems that an increase in density at nonequilibrium can only partially explain them since a larger increase was not observed when the nonequilibrium conditions were brought closer to the vapor pressure curve, like those seen in the Rayleigh line. Changes in the optical properties in the gas at nonequilibrium state may play a role in increasing the amount of scattered light collected by the imaging fibre optic probe. Furthermore, the range of scattering angles observed may also be changed at the nonequilibrium state. Therefore, until other probable contributions to the increase in the Brillouin components intensity are eliminated, we can not conclude that the change in the Brillouin line intensity seen in our experiment is due to sound bending in

the nonequilibrium gas. We had also observed a noticeable decrease in the Brillouin component frequency shift when the gas is in a nonequilibrium state. Although, the general theory by Schmitz and Cohen did mention a possible change in the Brillouin component line shape which would result in a change in the frequency shift when fluid is at nonequilibrium, we still cannot rule out the possibility of this change arising from the effect of having a higher density gas at the bottom of the cell or that a different range of scattering angles was observed when the gas is at nonequilibrium.

5.2 Conclusion

We have, for the first time to my knowledge, successfully utilized an imaging fibre optic probe to acquire a Brillouin spectrum of a gas. Using this technique, we can study the Brillouin scattering spectra of samples that have difficult to access or geometrically complicated scattering sites.

We have, through the use optical fibre technique, determined the sound speed in SF₆ gas at a pressure of 1.28 MPa (171 psig) to be $133 \pm 6 \text{ m s}^{-1}$. This agrees with results from other experiments which gives a sound speed of 136 m s^{-1} at 0.1 MPa. The changes in sound speeds with different pressures were also measured and compared with theoretical results based on the Virial equation corrected to the second coefficient. Our results are higher than the theoretical ones, about 15-30 m s^{-1} higher, and it also shows a higher degree of non-linearity than the theoretical results. This indicates an inadequacy in the sound speed relation derived from the Virial equation corrected only to the second virial coefficient.

We have also determined the linewidth of the Rayleigh line to be $50.5 \pm 4.8 \text{ MHz}$ and the Brillouin linewidth to be $54.8 \pm 4.8 \text{ MHz}$. Comparing the Brillouin linewidth from the computer simulation with the measured linewidth shows that they are of the same order of magnitude. This indicates that our computer simulation is able to simulate scattering conditions in the experiment that is close to the actual conditions.

Although the appearance of a set of unknown secondary peaks in the Brillouin spectrum had occupied a significant portion of our time in this experiment, we were nevertheless able to provide evidence that shows a strong indication of it coming from backscattering resulting from a secondary reflected laser beam.

We were able to observe effects in the Brillouin components of the spectrum at nonequilibrium that are similar to those predicted by the general theory of nonequilibrium fluids. These observed effects can not be attributed to nonlinear effects like sound bending until other possible causes of these effects can be eliminated. This would require further investigations to eliminate any optical effects that may contribute to the increase in intensity of the Brillouin components. We may conduct experiments with different temperature and sound speed gradients and compare any changes in intensities observed with those predicted by theory. One method of reducing optical effects in this experiment is to conduct this experiment with a binary gas mixture comprising of SF_6 and H_2 . Subjecting this binary mixture to a temperature gradient would tend to separate the gas into its constituent components, with H_2 on top and SF_6 at the bottom. At the boundary between these two regions, we should observe a large change in sound speed as we move from H_2 to SF_6 . In this case, the region of high sound speed gradient could be somewhere in the middle of the cell instead of being close to the bottom of cell, as was the case for this experiment. By observing scattering from a region in the middle of cell, the amount of parasitic light entering the collection optics from the exit window in the gas cell would be reduced.

Further improvements can be made to the imaging fibre optic probe to reduce noise and improve the finesse of the collection optics. Spatial filtering techniques may be employed to remove noise in the scattered light before it enters the imaging beam probe. This may also help to reduce any optical effects arising from the nonequilibrium gas. Smaller diameter optical fibres may also be used, so as to provide a better approximation to a point source for the spectral analysis optics. Improvements in the gas scattering cell can be made through the implementation of a temperature controlled heat source, insulation to the walls of the cell to reduce the effect of heat loss to the surrounding environment and finding ways to reduce scattering and reflections from the Mylar windows.

Although we had not been successful in confirming the existence of nonequilibrium effects caused by sound bending in a fluid subject to a temperature gradient, we have nevertheless laid the foundation for further studies into this problem. We had seen indications of the existence of these effects but could not at this time eliminate other factors that might also give rise to these effects. We performed a study into the variation of sound

speed with pressure and had observed a greater nonlinearity in the sound speed variation than was predicted by theoretical results derived from the Virial equation. We have developed a new method of scattered light collection for studies of spectra in the Brillouin scattering regime. With this method, we would be able to probe for sound waves coming from locations that would have otherwise been difficult to achieve if conventional optical techniques were used.

Bibliography

- [1] L. Brillouin *Ann. d. Phys.* **17**, 88, 1922.
- [2] L. I. Mandelstam *J. Rus. Phys.-Chem. Soc.* **58**, 381, 1926.
- [3] E.F. Gross *Nature(London)* **126**, 201, 400, 603, 1930.
- [4] C.S. Vankatesvaran *Proc. Ind. Acad. Sci. A* **15**, 316, 1942.
- [5] D.P. Mash, V.V. Morozov, V.S. Starunov, I.L. Fabelinskii, *Pis'ma Zh. Eksp. Teor. Fiz.* **2**, 562, 1965. [JETP lett. **2**, 1965].
- [6] T.J. Greytak, G.B. Benedek, *Phys. Rev. Lett.* **17**, 179, 1966.
- [7] I.L. Fabelinskii, *Uspekhi Fizicheskikh Nauk*, **164**, Issue 9, 897, 1994.
- [8] H. Kiefte, M.J. Clouter, R. Penny, *Phys. Rev. B* **30**, No. 7, 4017, 1984.
- [9] T.L. Andreeva *Physics Reports* **229**, No. 6, 291, 1993.
- [10] R. Schmitz, E.G.D. Cohen, *Physical Review A*, **35**, No. 6, 2602, 1987.
- [11] I. Procaccia, D. Ronis, I. Oppenheim, *Phys. Rev. Lett.* **42**, 287, 1979
D. Ronis, I. Procaccia, I. Oppenheim, *Phys. Rev. A* **19**, 1324, 1979.
- [12] T.R. Kirkpatrick, E.G.D. Cohen and J.R. Dorfman, *Phys. Rev. Lett.* **42**, 862, 1979;
44, 472, 1980; *Phys. Rev. A* **26**, 950, 1982; **26**, 972, 1982.
- [13] A.M.S. Tremblay, E. Siggia, M. Arai, *Phys. Lett.* **76A**, 57, 1980; *Phys. Rev. A* **23**, 1451, 1981.
- [14] G. Van der Zwan, D. Bedeaux, P. Mazur, *Physica* **107A**, 491, 1981.
- [15] L.S. Garcia-Colin, R.M. Velasco, *Phys. Rev. A* **26**, 2187, 1982.
- [16] D. Beysens, Y. Garrabos, G. Zalczer, *Phys. Rev. B*, **30**, 4017, 1980.
- [17] G. Satten, D. Ronis, *Phys. Rev. A*, **26**, 940, 1982.
- [18] T.R. Kirkpatrick, E.G.D. Cohen, *Phys. Lett.*, **78A**, 350, 1980; T.R. Kirkpatrick, E.G.D. Cohen and J.R. Dorfman, *Phys. Rev. A*, **26**, 995, 1982
- [19] I.M. Bortnik, *Gaseous Dielectr. Proc. Int. Symp., 3rd*, 533. 1982, editor: Loucas G. Christophorou.

- [20] T. Tanaka, G.B. Benedek, *Appl. Opt.*, **14**, 189, 1975.
- [21] R.B. Dyott, *Microwave Opt. Acoust.* **2**, 13, 1978.
- [22] H.S. Dhadwal, B. Chu, *Rev. Sci. Instrum.* **60**, No. 5, 845, 1989.
- [23] R.G.W. Brown, *Journal of Physics E*, **20**, 1312, 1987.
- [24] A.C. Eckbreth, *Appl. Opt.* **18**, 3215, 1979.
- [25] D.D Archibald, L.T. Lin, D.E. Honigs, *Applied Spectroscopy*, **42**, No. 8, 1558, 1988.¹
- [26] E.P. Ippen, R.H. Stolen, *Appl. Phys. Lett.* **21**, 539, 1972.
- [27] Y. Azuma, N. Shibata, T. Horiguchi, M. Tateda, *Electronics Letters*, **24**, No.5, 250, 1988.
- [28] J. Stone, A.R. Chraplyvy, *Electronics Letters*, **19**, No. 8, 275, 1983.
- [29] P.J.Thomas, N.L. Rowell, H.M. van Driel, G.I. Stegeman, *Physical Review B*, **19**, No. 10, 4986, 1979.
- [30] R.W. Tkach, A.R. Chraplyvy, R.M. Derosier, *Electronics Letter*, **22**, No. 19, 1011, 1986.
- [31] Oriel catalog II, *Precision Products for lasers and Optics*.
- [32] B. Chu, *Laser Light Scattering*, 2nd edition.
- [33] W.T. Welford, *Optics*, 2nd edition.
- [34] R. Guenther, *Modern Optics*.
- [35] Kirk-Othmer, *Encyclopedia of Chemical Technology*, 4th edition, 11, 428.
- [36] Hirschfelder, Curtiss and Bird, *Molecular Theory of Gases and Liquids*.
- [37] Private communications with Dr. John C. Lewis, Department of Physics, Memorial University of Newfoundland.
- [38] D. Balzarini, P. Palfy, *Can. Journal of Physics*, **52**, 2007, 1974.
- [39] W.T. Welford, *Aberrations of Optical Systems*.
- [40] G. Mahlke, P. Gossing, *Fiber Optic Cables*.

¹In this paper, the term "fibre optic probe" is used to describe plain optical fibres that are used without auxillary lenses or apertures for laser light delivery and scattered light collection.

- [41] E. Snitzer. *Journal of the Optical Society of America* **51**, No. 5, 491, 1961.
- [42] D. Marcuse. *Theory of Dielectric optical waveguides*
- [43] D. Glodge, *Apply Optics*, **10**, 2252, 1971.
- [44] Walter M. Elasser. *Journal of Applied Physics*. **20**, 1949.
- [45] Boon J.P , Yip , *Molecular Hydrodynamics*.
- [46] P.N. Segre, R.W. Gammon, J.V. Sengers, B.M. Law, *Physical Review A*, **45**, No. 2, 714, 1992.

Appendix A

The following are the physical properties² of sulphur hexafluoride, reproduced from [35] page 429.

Property	Value
Sublimation point, °C	-63.0
Heat of sublimation, kJ/mol ³	23.59
Triple point, °C	-50.52
Pressure at triple point, kPa ⁴	225.31
Critical temperature, °C	45.55
Critical pressure, MPa ⁵	3.759
Critical density, g.cm ³	0.737
Density, g/cm ³	
solid at -195.2 °C	2.863
liquid	1.336
gas	6.0886x10 ⁻³
Vapour pressure of saturated liquid, MPa ⁵	2.3676
Heat of formation, kJ/mol ²	-1221.66
Free energy of formation, kJ/mol ²	-1117.73
Heat of vaporization, kJ/mol ²	9.6419
Entropy, kJ/(mol.K) ²	291.874

²All data refer to 25°C and 101.3kPa (1atm), unless otherwise stated. To convert from atm to psia, multiply by 14.696.

³To convert J to cal, divide by 4.184.

⁴To convert kPa to mm Hg, multiply by 7.5.

⁵To convert Mpa to atm, divide by 0.101.

Property	Value
Heat capacity, J/(mol.K) ²	
liquid at -43 °C	119.5
gas	97.234
Surface tension at -20 °C , mN/m	8.02
Viscosity, mPa.s	
liquid	0.277
gas	0.01576
Thermal conductivity, W/(m.K)	
liquid	0.0583
gas	0.01415
Sound Velocity, gas, m/s	136
Refractive index. n	1.000783
Dielectric constant	
liquid	1.81
gas	1.00204

Appendix B

Propagative modes in an optical fibre

Propagative modes are present in an optical fibre because of interference effects in the fibre, arising from the coherent nature of the laser light. These constructive or destructive interferences give rise the effect of light travelling in the fibre only in precise angles; "precise" means that it propagates in directions in which the light waves will interfere constructively[40]. These different directions of propagation are shown in Figure A.1. The waves associated with the different paths of propagation are called modes (eigenwaves). The first ten modes of a multimode fibre (imaging from the output end of fibre) are shown in Figure A.2. Mathematically, these modes are solutions to Maxwell's equations in an optical waveguide. The number of modes in a glass core fibre (in the absence of birefringence) is approximately equal to

$$N = \frac{V^2}{2} \frac{g}{g+2}, \quad (\text{A.1})$$

where V is called the V number or the normalized frequency and g is the refractive index profile of the fibre, g is 1, 2 and ∞ for a triangular, parabolic and a step profile respectively [40]. The V number is given by $V = k a NA$, where k is wavenumber, a is the core diameter and NA is the numerical aperture. NA defines the maximum acceptance angle of the fibre which is related to the refractive indices as follows:

$$NA = \sin\theta_{\max} = \sqrt{n_1^2 - n_2^2}. \quad (\text{A.2})$$

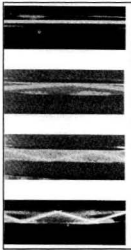


Figure A.1. Different modes, propagating down a dielectric bounded above and below by different media. [34]

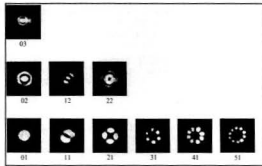


Figure A.2. The first ten $LP_{\nu\mu}$ modes, which can be seen from projections from end of a fibre.[40]

Therefore for a step index glass fibre, the maximum number of modes in the fibre is

$$N = \frac{V^2}{2} = \frac{k^2 a^2}{2} (n_1^2 - n_2^2) \quad . \quad (\text{A.3})$$

Thus, the following conditions (plus the launching conditions) affect the type and the number of modes present in an optical fibre; the numerical aperture, the core diameter and the frequency of the laser light used. When the V number is smaller than the constant $V_{c_1} = 2.405$ in a step index profile fibre, only a single mode, the HE_{11} mode can propagate in the core. V_{c_1} is the x value of the Bessel function $J_0(x)$ first zero.

The HE modes

The $HE_{\nu\mu}$ and $EH_{\nu\mu}$ modes are solutions of Maxwell's equation in a dielectric cylindrical waveguide that contain both nonzero H and E components along the direction of propagation. This is in contrast to the TE or the TM modes which have either a nonzero H or E component along the direction of propagation respectively. The nonzero H_z and E_z (assuming direction of propagation is in the z direction) arises from the

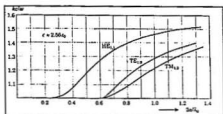


Figure A.3. The effect of fibre diameter on wave speed for the HE_{11} , TE_{10} and TM_{10} modes.

boundary conditions that are different from those of the conductive waveguide, for example, the electric field do not vanish in a dielectric as they do in a conductor. TE and TM modes can still exist in a cylindrical dielectric waveguide, but only in modes whose solutions does not have angular dependence. $HE_{\nu\mu}$ modes represents modes with a higher intensity in the H_z component compared to the E_z component, whereas the $EH_{\nu\mu}$ modes represent the opposite [41]. μ represents the order of Bessel's function in the solution and ν represents the roots of the μ th order characteristic equation of the HE or EH mode. In Figure A.3, it shows a plot³ of the wave speed versus the fibre diameter for the three modes, the HE_{11} , TE_{10} and the TM_{10} , in a cylindrical polystyrene rod. As the fibre diameter gets smaller, only the HE_{11} mode still persists. The dispersion of the HE_{11} mode (from the slope of the curve) is very small, therefore losses can be made very small.

Because of the near degeneracy between the $HE_{\nu,1,\mu}$ and the $EH_{\nu,1,\mu}$ modes, we have a case of superposition of these two modes[42]. Glodge [43] introduced the notation of $LP_{\nu\mu}$ modes in this case to suggest "linearly polarized modes". The HE_{11} mode is also the LP_{01} mode.

³From numerical calculations by Elasser for roots $\mu=0$ and 1. [44]

Appendix C

Inelastic Light Scattering[34]

To quantum mechanically describe Brillouin scattering, we can consider the interaction of an incident photon, a scattered photon and a phonon in an inelastic scattering process. There are two types of inelastic scattering processes that can take place:

i) absorption; An incident photon of energy $\hbar\omega_p$ collides with a phonon of energy $\hbar\omega_s$ to produce a photon of energy $\hbar\omega_d$ from the scattering site. The phonon is destroyed in this process. This process satisfies the following equations:

$$\hbar\omega_p + \hbar\omega_s = \hbar\omega_d \quad (\text{A.4})$$

or

$$\vec{k}_p + \vec{k}_s = \vec{k}_d \quad (\text{A.5})$$

\vec{k}_p , \vec{k}_s and \vec{k}_d are wavevectors of incident photon, incident phonon and scattered photon respectively, as shown in Figure A.4.

ii) emission; An incident photon of energy $\hbar\omega_p$ enters the scattering site and produces both a photon of energy $\hbar\omega_d$ and a phonon of energy $\hbar\omega_s$ from the scattering site, such that

$$\hbar\omega_p = \hbar\omega_d + \hbar\omega_s \quad (\text{A.6})$$

$$\vec{k}_p = \vec{k}_d + \vec{k}_s \quad (\text{A.7})$$

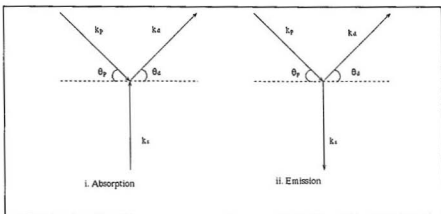


Figure A.4 Inelastic light scattering

The phonons in both cases are either naturally present (as Fourier components of the thermal noise) or are externally generated. In both the absorption and emission scattering, a frequency shift occurs. From Equations (A.5) and (A.7) we can see that the momentum transfer is $\hbar\vec{k}_p - \hbar\vec{k}_d = \pm\hbar\vec{k}_s$, therefore the wavelength of the momentum transferred is the wavelength of the phonon.

We can rearrange the vectors in Figure A.4 to the form as shown in Figure A.5. From Figure A.5, the x-components of both (i) and (ii) are

$$k_p \cos\theta_p = k_d \cos\theta_d, \quad (\text{A.8})$$

$$k_p \cos\theta_p - k_d \cos\theta_d = 0. \quad (\text{A.9})$$

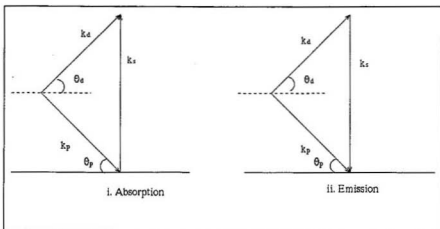


Figure A.5 Vector addition

The y-components for (i) are

$$-k_p \sin \theta_p + k_s = k_d \sin \theta_d \quad (\text{A.10})$$

and for (ii) are

$$-k_p \sin \theta_p = k_d \sin \theta_d - k_s \quad (\text{A.11})$$

From Equations (A.9), (A.10), and (A.11), we can analyse the resulting wavevectors from the photon, phonon interaction in both the emission and absorption process.

Since the frequency shift in the scattered light is small, we can approximate that

$k_p = k_d$. From (A.8), we have $\theta_p \approx \theta_d$, we

can then write (A.10) as ,

$$k_x = 2k_p \sin\theta_p \quad . \quad (\text{A.12})$$

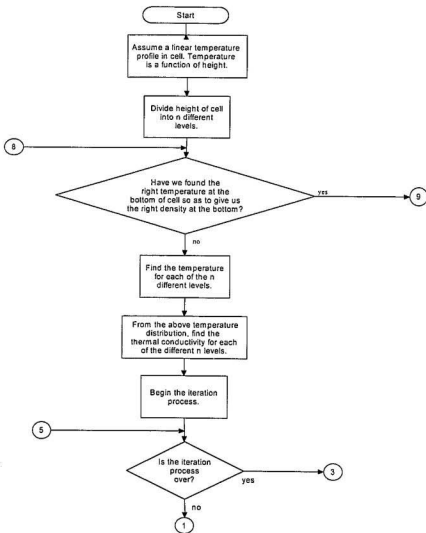
If the angle between the scattered and the unscattered photon (i.e. direction of photon if no deflection occurred) is θ , then θ_p is equal to $\theta/2$. Let the incident photon wavelength be λ_0 , and the phonon wavelength be λ , we can then rewrite (A.12) as the following,

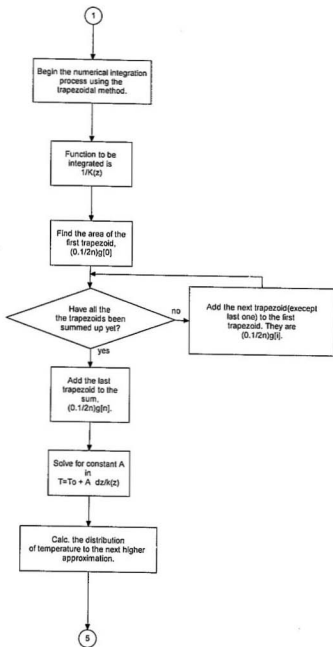
$$\frac{2\pi}{\lambda} = \frac{4\pi}{\lambda_0} \sin\left(\frac{\theta}{2}\right) \quad , \quad (\text{A.13})$$

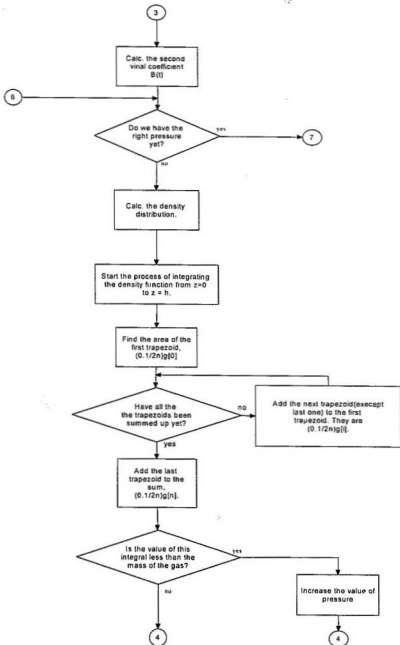
therefore we have $\lambda = \lambda_0 / 2 [\sin(\theta/2)]^{-1}$.

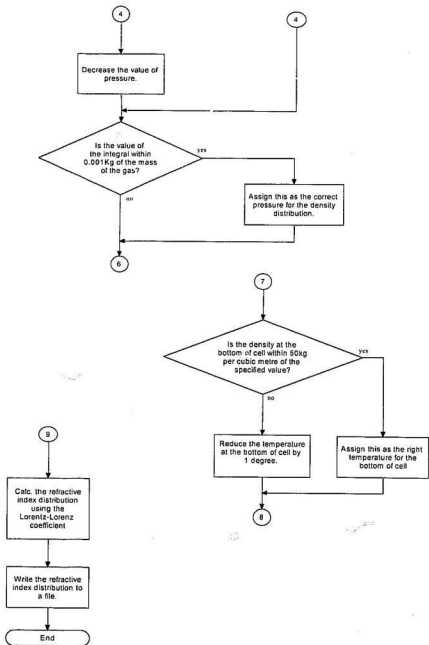
APPENDIX D

Flowchart for calculations of density distribution in a temperature gradient.









Source Codes for calculations of density distribution in a temperature gradient.

(Written in MapleV)

```
restart;
n := 100;
s := 15:# specify the no. of iterations to be performed before the temperature distribution
converges.
kappa1 := array(1..(n+1));
z1 := array(1..2*(n+1));
TT := z -> ((T1 - T0)/h)*z + T0: # Assume a linear temperature profile in first
approximation
TT(z):
T0 := 30: # Temperature (in kelvins) at bottom of cell.
T1 := 300:# Temperature at top of cell.
Ttrp := 222.35:# Triple point of sulphur hexafluoride.
mm := 0.146:#molecular weight of sulphur hexafluoride in kg per mole.
h := 0.08: # height of cell in metre.
Tc := 318.55:#critical temperature of sulphur hexafluoride
Pc := 3.759:# critical pressure of sulphur hexafluoride
kappa := z -> 4.84*10^(-5)*(TT(z)^0.85)*(1 + 3.35*exp(-Ttrp/TT(z))): #Thermal
conductivity as a function of height
kappa(z):
kappa2 := t -> 4.84*10^(-5)*(t^0.85)*(1 + 3.35*exp(-Ttrp/t)): #Thermal conductivity as
a function of temperature
B := 0.08;
for i from 1 by 1 to (n+1) do:
    z1[i] := (B*(i-1))/n : #Divide height in n different levels.
    z1[i+n+1] := (B*(i-1))/n :
od:
rho := array(1..(n+1));
N := array(1..(n+1));
```

```

T := array(1..(n+1));
A := array(1..s);
Mx := array(1..(n+1));
g := array(1..(n+1));
wx := 20;
for w from 1 by 1 to wx do: # this is for finding the right T0
for i from 1 by 1 to (n+1) do :
z := z1[i];
kappa1[i] := kappa(z): # find the thermal conductivity for different heights.
od:
for k from 1 by 1 to s do: #do s number of iterations
for i from 1 by 1 to (n+1) do: # integrate function using n number of trapezoids.
g[i] := (kappa1[i])^(-1); # function to be integrated
od:
g[1] := 0: #Boundary condition for T(z), since at z=0, temperature is T0 means that
integral is zero which implies that the integrand is zero.
T[1] := (B/(2*(n+1)))*g[1]: # first trapezoid.
for i from 2 by 1 to (n) do:
T[i] := T[1] + sum((B/(2*(n+1)))*2*(g[j]^2),j=2..i): # summing up all the trapezoids
od:
T[n+1] := T[n] + (B/(2*(n+1)))*g[n+1]: # add the last trapezoid to the rest.
for i from 1 by 1 to (n+1) do:
g[i] := T[i] : #reuse array g[i].
od:
solution := solve( {T1 = T0 + A[k]*T[n+1]}, { A[k]}): #find constant A for this
iteration.
assign (solution):
for i from 1 by 1 to (n+1) do :
T[i] := evalf(T0 + (A[k]*g[i])): #find the temperature distribution for the next higher
approximation

```

$\kappa_{1[i]} := \kappa_{2}(T[i])$; # and the also the thermal conductivity distribution for this higher level of approximation.

od:

od:

A := 'A';

BT := t -> B0 - (A0)/(R*t) - c/t^3 : # the second virial coefficient

A0 := 1.064*10^(-6);

B0 := 2*10^(-4);

c := 1.24*10^3);

Rho := t -> (p*mm)/(R*t*(1 + BT(t))); # density as a function of pressure, temperature and the second virial coefficient.

R := 8.314*10^(-6);

p := 1.9; #in MPa.

Mv := 0.040; # total mass of gas in cell in Kg.

q := 10;

for k from 1 by 1 to q do: #do q number of iterations to find the right pressure
for i from 1 by 1 to (n+1) do :

t := T[i];

rho[i] := Rho(t); # find the thermal conductivity for different heights.

od:

for i from 1 by 1 to (n+1) do: # integrate the density function using n number of trapezoids.

g[i] := rho[i]*0.0045; # function to be integrated

od:

Mx[1] := (B/(2*(n+1)))*g[1]; # first trapezoid.

for i from 2 by 1 to (n) do:

Mx[i] := Mx[1] + sum((B/(2*(n+1)))*2*(g[j]),j'=2..i); # summing up all the

trapezoids

od:

Mx[n+1] := Mx[n] + (B/(2*(n+1)))*g[n+1]; # add the last trapezoid to the rest.

```

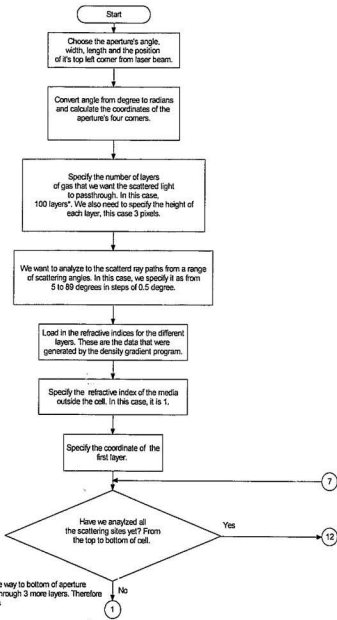
My := Mx[n+1] - Mv; # difference between the mass from the integrated function and
the actual mass
if (My < 0 ) then
p := p + 0.05 # if it is lower than actual mass, increase pressure
else p := p - 0.05 #if it is higher than actual mass, decrease pressure
fi:
if abs(My) < 0.001 then

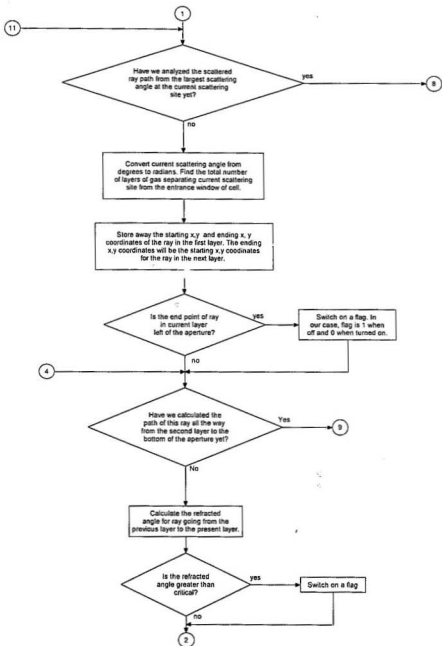
k := q # if mass is within 0.001 Kg, then we have got a pressure that satisfy the mass
conservation requirement.
fi:
od:
Ry := rho[1] - 1200; # difference between the computed density at bottom of cell and
what we want it to be.
if abs(Ry) < 50 then w := wx # if the computed density is within 50 Kg of the density
specified, then we got the right T0
fi:
T0 := T0 - 1; # if computed density doesn't fall within 50Kg of the density specified,
then decrease T0 by 1 degree.
print (T0):
od:
L := 0.0783*10^(-3);# Lorentz-Lorenz coefficient
readlib(write):
open(index): # open file to write data.
for i from 1 by 1 to (n+1) do:
t := T[i]:
rho[i] := Rho(t);#density at different temperatures.
N[i] := sqrt((2*L*rho[i] + 1)/(1 - L*rho[i])); # refractive index at different temperatures.
writeln(N[i]); # write refractive index data to file.

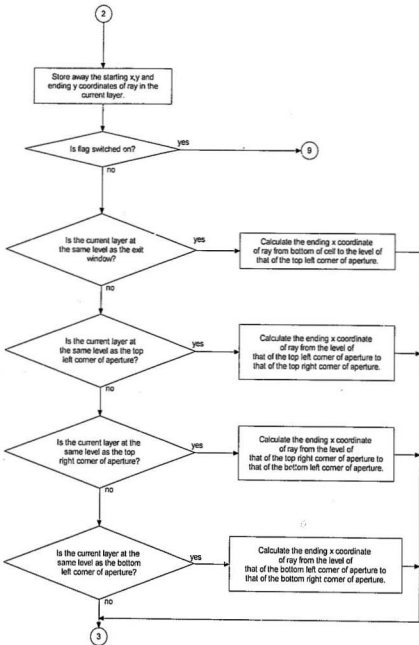
```

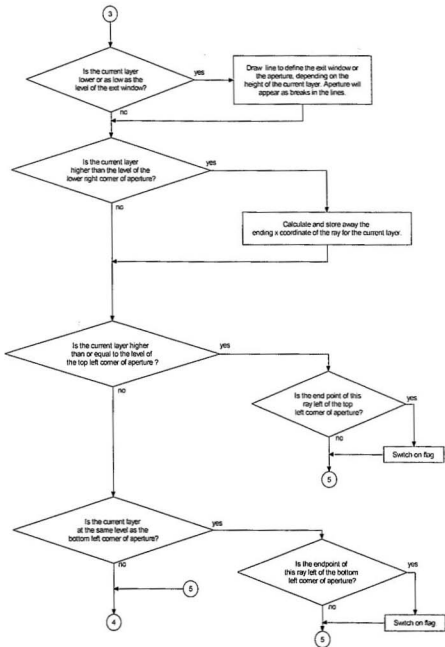
```
od:
close(): #close file
print (rho[1]); print(rho[101]);
plot([ [z1[m + n+1] , N[m]] $ m = 1..(n+1)]); # plot height against the refractive indices.
plot([ [z1[m + n+1] , T[m]] $ m = 1..(n+1)]); #plot height against the temperature
plot([ [z1[m + n+1] ,rho[m]] $ m = 1..(n+1)]); #plot height against the density
plot([ [T[m] ,rho[m]] $ m = 1..(n+1)]); #plot temperature against the density
```

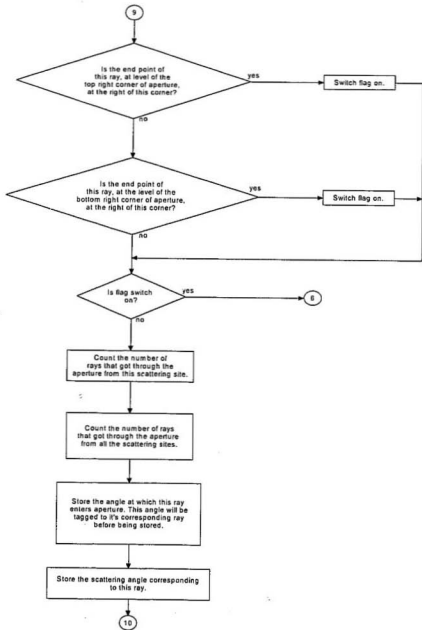
Flowchart for tracing of scattered rays through a density gradient.

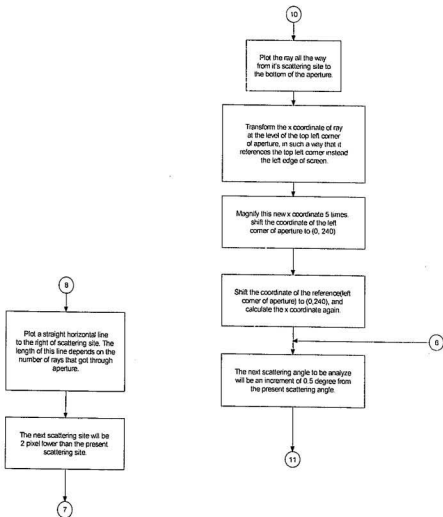


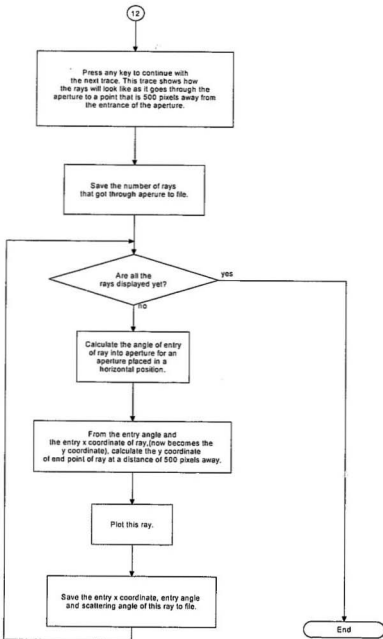












Source codes for tracing of scattered rays through a density gradient. (Written in TurboC++)

```
#include <graphics.h>
#include <conio.h>
#include <math.h>
#include <iostream.h>
#include <fstream.h>

class draw {
public:
    float stx, sty, x, phi;
    int height, edy, borderstr, borderend, bordery ;
    draw(int y); //constructor
    void border();
    void ray();
    int angcalc(float n, float n2, int *m);
};

draw::draw(int y)
{ stx = 500 ;
  sty = y ;
  height = 3 ; // height of the layer
  borderstr = 1;
  borderend = 639;
}

void draw::border()
{
    setcolor(4);
    line(500, 0, 500, 479); // draw laser path
```

```

line(borderstr, bordery, borderend, bordery);
}

void draw::ray() // calculate the x coord. of end point of refracted ray
{
x = stx - ((edy - sty)*tan(phi));
}

int draw::angcalc(float n, float n2, int *m) //calc refracted angle
{
//edy is call by reference
stx = x; //the end point (x) is now the starting point of ray
sty = edy; // similarly for the y coord. of ray
*m = *m + height; /*increment the value of edy at it's
memory location my height, this is where the next ray's y coord
would end */

float t, t1;
t = (n*sin(phi));
t1 = (float) t/n2; //calc the refracted angle of next ray
if(t1 > 1) return 0; // if greater than critical angle, end here
phi = asin(t1);
return 1;
}

main()
{ float inp_ang, lxmin, lxmax, lymin, lymax, llymin, llxmin, llymax, llxmax;
int apwidth, aplength;
lymin = 400;//Y coord of top left corner

```

```

cout << "enter the aperture's angle: " ;
cin >> inp_ang;
cout << "enter the aperture's width and length: " ;
cin >> apwidth >> aplength;
cout << "enter the aperture's horizontal distance from beam: " ;
cin >> lxmin; //X coord of top left corner

inp_ang = (float) (22*inp_ang)/(7*180);
    // followings are coord of the aperture
lxmax = lxmin + (apwidth*cos(inp_ang)); //X coord. of top right corner
lymax = lymin + (apwidth*sin(inp_ang)); //Y coord. of top right corner
llxmin = lxmin - (aplength*sin(inp_ang)); //X coord of bottom left corner
llymin = lymin + (aplength*cos(inp_ang)); //Y coord of bottom left corner
llxmax = llxmin + (apwidth*cos(inp_ang)); //X coord of bottom right corner
llymax = llymin + (apwidth*sin(inp_ang)); //Y coord of bottom right corner

ofstream out("refrac.dat"); // open file for output

if (!out) {
    cout << "Cannot open file for data"; // check for file integrity
    return 1;
}

int driver, mode;

driver = VGA;
mode = VGAHI;
initgraph(&driver, &mode, " ");
floodfill(100, 100, 1);

```

```

int a, j, k, m, b, ystart, y0, ymax, ystep, test, layers, ang_mark, ray_trk;
float i, t2, n[150], ang, max, ang_step, sx[150], sy[150], ex[150], ey[150];
float ang_deg[200], ang_stor[200], x_stor[200], phi22, hg_stor[200];

```

```

layers = 100; // compute the ray path through a 100 layers
ang_step = 0.5; // change scattering angles in steps of 0.5 degrees
y0 = 50; // start ray tracing from Y coord of 50
ystart = y0;
ystep = 2; // change scattering site position by 2
draw obl(y0); // initialize the drawing procedure
ymax = y0 + (layers)*(obl.height); // this is the position of the exit window
ray_trk = 0;

```

```

obl.bordery = y0; // draw the entrance.
obl.border();

```

```

ifstream fin("index.dt"); // open refractive index data file
if(!fin) { // check it's integrity
    cout << " Cannot open inout file. \n";
    return 1;
}

```

```

for (k = 0; k < layers ; k++)
{
    b = 99 - k; // have to load in data in reverse because data was calc
    fin >> n[b]; // with the lowest temp first
}

```

```

fin.close(); // close data file
for (k = layers; k < (layers + 4) ; k++)
{
n[k] = 1.00;
}

while (y0 < ymax) // calc ray paths from top to bottom of cell
{
ang = 5; //minimum angle
max = 89; //maximun angle
ang_mark = 0; // keep track of the no. of rays going through aperture
// from each scattering site
while ( ang < max ) // calc ray path from angles 0 to 89 at each site.
{
m = 0;
draw obl(y0);
obl.phi = (float) (22*ang)/(7*180);// convert to radians
a = (y0 - ystart)/obl.height; /* calc no. of layers bet. present site
and the entrance window */
obl.edy = ystart + ( a + 1)*obl.height;/* this is the end (Y) of ray in
first layer from current site, which is just the Y position of the next layer */
sx[m] = obl.stx;// store away the start(x) of this ray in first layer
sy[m] = obl.sty;// store away the start(y) of this ray
ey[m] = obl.edy;// store away the end (y) of this ray
setcolor(a);
obl.ray(); // calc the end(x) of this ray in first layer
ex[m] = obl.x; // and store it away
if (ex[m] < lxmin) {test = 0 ;
a = layers + 5;} // if this ray is left of aperture,
else test = 1; // don't plot
}
}

```

```

if (a > layers) test = 0;

for(j = a ; j < (layers + 3) ; j++) // calc the ray path through
{
    // different layers from current site at current angle
    m++;

    test = obl.angcalc(n[j], n[j+1], &obl.edy); //address of obl.edy is passed
    // and is calc refracted angle greater than the critical angle
    sx[m] = obl.stx; // store away the start(x) of ray in current layer
    sy[m] = obl.sty; // store away the start(y) of ray in current layer
    ey[m] = obl.edy; // store away the end(y) of ray in current layer
    if (!test) j = (layers + 3); // do the following if angle is less than critical
    else {
        if (j == (layers - 1)) {obl.edy = lymin; // trace ray from exit
            ey[m] = lymin; obl.borderend = lxmin;} //window to aperture (top
            // left)
        if (j == (layers)) {obl.edy = lymax; // trace ray from top left
            ey[m] = lymax; obl.borderstr = lxmax;} // to top right of aperture
        if (j == (layers + 1)) { obl.edy = llymin; // trace ray from top right
            ey[m] = llymin; obl.borderend = llxmin;} // to bottom left of
            // aperture
        if (j == (layers + 2)) {obl.edy = llymax; //trace ray from bottom
            //left
            ey[m] = llymax; obl.borderstr = llxmax;} // to bottom right of
            // aperture
        if (obl.edy > (ymax - obl.height)) {
            obl.bordery = obl.edy; // draw exit window
            obl.border();
        }
    }
}

```

```

ob1.borderstr = 1; // reinitialize these
ob1.borderend = 639; // two variables
setcolor(a); // colour my ray
if (j < (layers + 3)) {
    ob1.ray(); // calc and store away the end(x) of
    ex[m] = ob1.x; // ray in current layer
    if (j < layers) {
        if (ex[m] < lxmin) {test = 0; // is ray left of top left corner
            j = layers + 3; // of aperture
        }
        else if (j == (layers + 1)) {
            if (ex[m] < llxmin) {test = 0; j = layers + 3;}
        } // is ray left of bottom left corner of aperture
    }
}

k = m - 2;
if (ex[k] > lxmax) {test = 0; } // is ray right of top right corner
else if (ex[m] > llxmax) {test = 0; } // is ray right of bottom right corner of
// aperture
if (test == 1) { //plot only those rays that got through the aperture
    ang_mark++; // one more ray got through
    ray_trk++; //track the total no. of rays that had went through
    ang_stor[ray_trk] = ob1.phi; // stor angle in which ray enters aperture
    ang_deg[ray_trk] = ang; //stor scat angle of ray that enters aperture
    hg_stor[ray_trk] = y0;
    k = m - 3;
    x_stor[ray_trk] = (ex[k] - lxmin)*5 + 240;
    /*position of ray across aperture. Transfer this to vertical position
    and shift it down by 240 pixels. Store it */

```

```

for(j = 0; j < (m + 1) ; j++)
    {
        obl.stx = sx[j];
        obl.sty = sy[j];
        obl.x = cx[j];
        obl.edy = ey[j];
        line(obl.stx,obl.sty,obl.x,obl.edy); //plot 'em rays
    }
}
ang = ang + ang_step; //next scattering angle
}
obl.bordery = y0; // show the number of rays
obl.borderstr = 500; // that got through the aperture
obl.borderend = ( 500 + (10*ang_mark)); // for each scattering site
obl.border(); // for all angles
y0 = y0 + ystep ; //next scattering site
}
outtextxy(10,20, "Press any key to continue with trace");

getch();
// restorecrtmode();

cleardevice(); //prepare for next screen

```

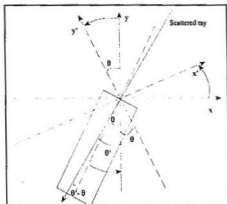


Figure A. 6 Transformation of entry angle from an aperture in an angled position to one in a vertical position. For a horizontal position, interchange x and y coordinates.

```

floodfill(100, 100, 1);
setcolor(4);
line(0, 200, 160, 200);

float gamma;

out << ray_trk << "n";

for(j = 1; j < ray_trk; j++)
{
    ob1.sty = x_stor[j];
    ob1.phi = ang_stor[j];
    gamma = ob1.phi - inp_ang ; //tilt aperture and rays to horizontal position
    ob1.edy = ob1.sty - 500*tan(ob1.phi - inp_ang);//plot rays to end at 500 pixels
    setcolor(j);
}

```

```

line( 0, ob1.sty, 500, ob1.edy);
cout << hg_stor[j] << " " << " " << " ";
out << ob1.sty << " " << gamma << " " << ang_deg[j] << "\n" ;
/* stor the entry position, angle and scattering angle of ray for tracing
through probe later.*/
}
line( 0, 240, 639, 240);
line(0, 250, 639, 250);
line(0, 260, 639, 260);

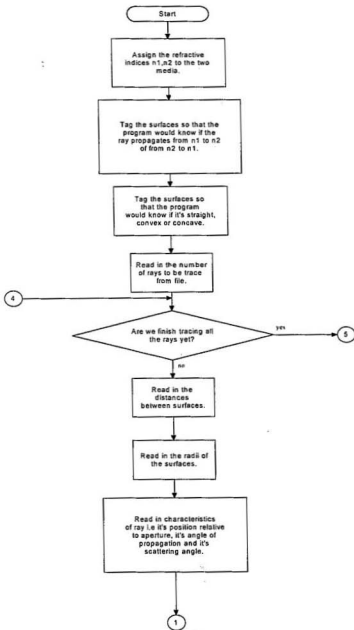
getch(); //press any key to end

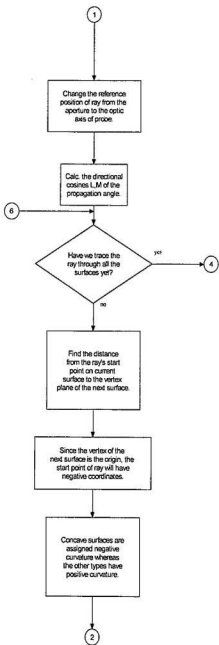
restorecrtmode(); //restore screen

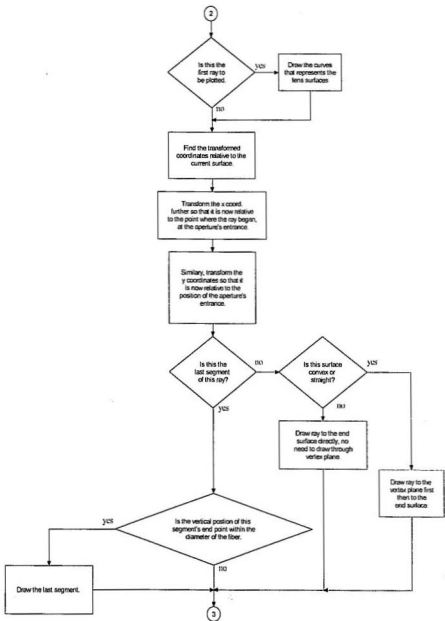
/* for (j = 1; j < ray_trk ; j++)
{
    cout << ang_deg[j] << " " << j << " ";
}
*/
out.close(); //close output file
return 0;
}

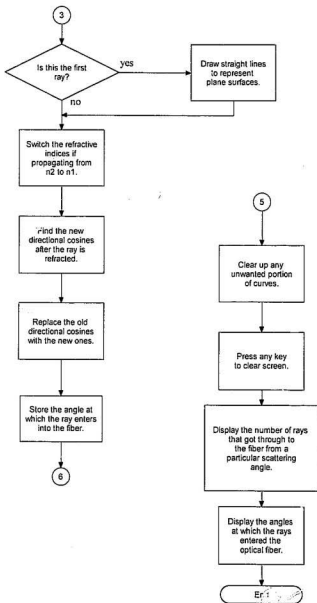
```

Flowchart for tracing of scattered rays through imaging fibre optic probe.









Source codes for tracing of scattered rays through imaging fibre optic probe.(Written in TurboC++)

```
#include <graphics.h>
#include <conio.h>
#include <math.h>
#include <iostream.h>
#include <fstream.h>

class trace {
public:
    float x0, y0, x, y, phi2, G, F, del, tmp, cos1, cos2, K, L2, M2;
    trace(float y3); //constructor
    void transfer(int x_1, int y_1, float c, float L, float M);
    void refrac(float n1, float n2, float L, float M, float c);
};

trace::trace(float y3) //specify the x,y coord. of the start point of ray
{
    y = y3;
    x = 0;
}

void trace::transfer(int x_1, int y_1, float c, float L, float M)
//this transfer function transform the coord from one surface to the next
{
    tmp = (float) (M/L)*(0 - x_1);
    y0 = y_1 + tmp; //calc the x,y coord of ray at the plane at the
    x0 = 0; // vertex of lens, the vertex is at the origin.
    G = L - (c*y0*M);
    F = c*(y0*y0);
```

```

tmp = G + sqrt(G*G - c*F);
del = (float) (F/tmp); //calc the length of ray from plane to surface of lens
x = L*del;           // above length along the x-axis
y = y0 + M*del;     // above length along the y-axis
}

void trace::refrac(float n1, float n2, float L, float M, float c)
// this refraction function calc the refracted directional cosines of ray
{
cosl = sqrt(G*G - c*F) ;
tmp = sqrt(n2*n2 - n1*n1*(1 - cosl*cosl)) ;
cosl2 = (float) (tmp/n2);
K = n2*cosl2 - n1*cosl;
tmp = n1*L + K - c*K*x ;
L2 = (float) (tmp/n2) ; //refracted directional cosine L
tmp = n1*M - c*y*K ;
M2 = (float) (tmp/n2); //refracted directional cosine M
}

main()
{
ifstream fin("refrac.dat");//open file 'refrac.dat'. Data in file to be read
if(!fin) { //check integrity of file
cout << "cannot open input file. \n";
return 1;
}
float assign, temp3, deg_ang;

int driver, mode;
driver = VGA;

```

```

mode = VGAHI;
initgraph(&driver, &mode, " ");
floodfill(100, 100, 1);

setcolor(4);
line(1, 250, 639, 250); //draw optic axis

int d[20], dtmp, i, j, m, x_1, y_1, ymax, ystep, rad[20], h, surf[20], power[20];
float t2, n[4], ang, max, c, L, M, w, track_ang[1000], track_M[1000];
float xt_1, yt_1, xt0, yt0, xt, yt;
float n1, n2, temp;
int track, num_ray;

n1 = 1.00;
n2 = 1.52; //refractive index of lens

h = 250; //vertical position of the optic axis
track = 0; // track the number of rays that will get thru. to fibre

surf[4] = 1; // this specifies that ray is going from air to glass
surf[5] = -1; // this specifies that ray is going from glass to air
surf[6] = 1;
surf[7] = -1;
surf[8] = 1;
surf[9] = -1;
surf[10] = 1;
surf[11] = -1;
surf[12] = 1;

```

```

power[4] = 1; // for straight and convex(curve left) surface, power is 1
power[5] = -1; //for concave(curve right) surface, power is -1
power[6] = 1;
power[7] = 1;
power[8] = 1;
power[9] = -1;
power[10] = 1;
power[11] = 1;
power[12] = 1;

```

```

for (j = 1; j < 1001; j++){
    track_ang[j] = 0; //set all elements in these arrays to zero
    track_M[j] = 0;
}

```

```

fin >> num_ray; //get the total number of ray to be plotted from file

```

```

for (j = 1; j < num_ray; j++)
{
    setcolor(j);
    d[4] = 160; //distance from start(aperture entrance) to 1st surface of lens 1
    d[5] = 25; //distance from 1st to 2nd surface of lens 1
    d[6] = 80; //distance from 1st to 2nd (biconvex)lens
    d[7] = 36; //distance from 1st surface to middle of biconvex lens
    d[8] = 0; // two plano-convex lens place back to back
    d[9] = 36; //distance from middle to 2nd surface of biconvex lens
    d[10] = 80; //distance from 2nd to 3rd lens
    d[11] = 42; // distance from 1st to 2nd surface of lens 3
    d[12] = 60; //distance from 3rd lens to end of ray
    rad[4] = 10000; //straight surfaces have radii of 10000
}

```

```

rad[5] = 488; // 4 & 5 make a plano-convex lens
rad[6] = 143; // 6 to 9 make a biconvex lens
rad[7] = 10000;
rad[8] = 10000;
rad[9] = 143;
rad[10] = 124; // 10 & 11 make another plano-convex lens
rad[11] = 10000;
rad[12] = 10000; // this is the plane where all the rays end
fin >> assign >> temp3 >> deg_ang; // read in the characteristics of ray, such as
// relative starting position, angle and its scattering angle.
assign = assign - 250; // shift the reference position of rays to the optic axis
trace obl(assign);

xt = 0;

obl.phi2 = -temp3; // angles of the rays is reversed
L = cos(obl.phi2); // directional cosine L of ray
M = sin(obl.phi2); // directional cosine M of ray

for (i = 4; i < 13; i++)
{
    d[i] = d[i] - obl.x; // dist. of ray from start surface to vertex of end surface
    x_1 = -d[i]; // vertex of end surface is the origin
    y_1 = obl.y; // " "
    c = (float) 1/rad[i]; // curvature of surface, positive for convex
    c = c*power[i]; // negative for concave

```

```

if ( j < 2 ) { //--
if ( power[i] < 0 ) { //|
arc(xt + d[i] - rad[i], h, 312, 48, rad[i]); //| draw the curves
} //| -for the lenses,
else //| only once
{arc(d[i] + rad[i] + xt , h, 132, 228, rad[i]);//|
} //|
} //--
obl.transfer(x_1, y_1, c, L, M); //calc the transformed x,y coord.

```

```

xt_1 = x_1 + d[i] + xt; //x-coord. of ray at start surface
xt0 = obl.x0 + d[i] + xt; //coord. of ray at vertex plane
xt = obl.x + d[i] + xt; // coord. of ray at end surface

```

```

yt_1 = y_1 + h; //y-coord. of ray at start surface
yt0 = obl.y0 + h; //coord. of ray at vertex plane
yt = obl.y + h; // coord. of ray at end surface

```

```

if ( i < 12 ) { //draw ray all the way thru. except the last
    if ( power[i] < 0 ) { //if surface is concave, draw to end surface
        line(xt_1, yt_1, xt, yt); //directly
    }
    else {
        line(xt_1, yt_1, xt0, yt0); //if surface is convex, draw to vertex
        line(xt0, yt0, xt, yt); //plane then to end surface.
    }
}
else

```

```

    {
    if ( yt>237 && yt<263) { // draw the last segment of the ray only
    track++;          //if the y-coord of ray falls within the
    line(xt_1, yt_1, xt, yt); // diameter of the optic fibre
    deg_ang = deg_ang*10; //for a particular scattering angle, this number
    track_ang[deg_ang]++; //of rays was able to get thru. to the fibre
    }
}
if (j < 2) {
    if (rad[i] == 10000){ //draw straight lines for plane surfaces
    line(xt , 170, xt , 330);
    }
}
if (surf[i] > 0) { //going from air to glass
n1 = 1.00;
n2 = 1.52; }
else { //going from glass to air, switch the refractive indices
n1 = 1.52;
n2 = 1.00;
}
obl.refrac(n1, n2, L, M, c); //calc the new directional cosines
M = obl.M2; // use the new directional cosines for the next transformation
L = obl.L2;
if (i == 11) { // find the angles at which ray go into fibre
temp = acos(M);
temp = (float) (180*7*temp)/22;
track_M[j] = temp - 90 ;
}
}
}

```

```

setcolor(1);
int rectangle[] = {0,0, 639,0, 639,170, 0,170, 0,0},
npts = sizeof(rectangle)/(2*sizeof(int));           //-|
                                                    //|
fillpoly(npts, rectangle);                          //| use this
                                                    //|- section

int rectangle2[] = {0,330, 639,330, 639,479, 0,479, 0,330};//| to clear
npts2 = sizeof(rectangle2)/(2*sizeof(int));         //| unwanted
                                                    //| portions
fillpoly(npts2, rectangle2);                        //-| of curves

line(0,240, 160,240); //draw aperture (top)
line(0, 260, 160, 260);//draw aperture (bottom)
getch(); //press any key to clear screen
restorecrtmode();

for (j = 1 ; j < 1000 ; j++) { //display the number of rays that got
    if(track_ang[j] != 0) { // thru. to the fibre for a particular
        deg_ang = (float)j/10 ; // scattering angle
        cout.width(5);
        cout << deg_ang ;
        cout.width(5);
        cout << track_ang[j] << " ";
    }
}

for (j = 1 ; j < num_ray; j++){//display the angles at which the rays enters
    cout << track_M[j] << " "; // the optic fibre
}

fin.close(); //close file

return 0; }

```